Stochastic Environmental Research and Risk Assessment (2020) 34:2179–2210
https://doi.org/10.1007/s00477-020-01880-3

ORIGINAL PAPER

Dehesa environment mapping with transference of a Random Forest classifier to neighboring ultra-high spatial resolution imagery at class and macro-class land cover levels

Laura Fragoso-Campón[1] · Elia Quirós[1] · José Antonio Gutiérrez Gallego[1]

Accepted: 19 September 2020 / Published online: 6 October 2020

Abstract

Accurate vegetation cover maps of forested areas are crucial for ecosystems monitoring, as well as for management of water balance, flood and fire risk, and other forest-associated resources. With this regard, remote sensing techniques have been used for land cover mapping worldwide. Here, we propose a vegetation-mapping methodology in a *dehesa* environment using ultra-high spatial resolution imagery (UHSR) with a spatial resolution of 0.25 m and four bands in the visible and near-infrared spectrum. Land cover categories were defined by their runoff generation capability and considered two levels of disaggregation: among species (macro-class level) and within species (class level). Additionally, we developed a method to reduce field campaigns and manual work by transferring random forest classifiers trained with a group of images (training group) to neighboring images (validation group). The training group was remarkably accurate, achieving an overall accuracy of 91.6% (k = 0.89) at the class level and 95.8% (k = 0.94) at the macro-class level. The results for the validation group were also very high, with an overall accuracy of 78.3% (k = 0.74) at the class level and 86.3% (k = 0.82) at the macro-class level. Moreover, we found that the blue band, soil color index, and texture features have a great influence on species discrimination, especially within shrub species in *dehesa* environments. Notably, having accurate land cover maps is crucial, given that the use of a global database led to underestimating the potential runoff in the most representative land cover in the *dehesa* environment. Future research will focus on the automatic generation of new samples extracted from the classified UHSR images, which could be used as training datasets for the supervised classification of other high spatial resolution images (e.g., Sentinel imagery) for regional-scale hydrological models.

Keywords Jeffries–Matusita distance · National Plan of Aerial Orthophotography (PNOA) · Run off · Shrub · Training-data · Tree grass ecosystem

1 Introduction

Accurate vegetation maps of forested areas are widely known to be crucial for forest management. Notably, vegetation cover has a great influence on biodiversity and ecosystem monitoring (Fang et al. 2018), water balance models (Becker et al. 2019; Dias et al. 2015; Dionizio and Costa 2019; Lima de Almeida et al. 2019), hydrological modeling and flood management (Chen et al. 2019a; Chymyrov et al. 2018; Dou et al. 2018; Fragoso-Campón et al. 2019; Melesse and Shih 2002; Niu and Sivakumar 2014; Van der Sande et al. 2003), soil erosion (Eroğlu et al. 2010), fuel type (García et al. 2011; Lasaponara and Lanorte 2007a; Riaño et al. 2007), and associated forest resources and biomass inventories (Castillo et al. 2017; Fassnacht et al. 2017; Garcia et al. 2017; Hawryło and

Electronic supplementary material The online version of this article (https://doi.org/10.1007/s00477-020-01880-3) contains supplementary material, which is available to authorized users.

✉ Laura Fragoso-Campón
laurafragoso@unex.es

Elia Quirós
equiros@unex.es

José Antonio Gutiérrez Gallego
jagutier@unex.es

[1] Department of Graphic Expression, Universidad de Extremadura, Escuela Politécnica, Avda. Universidad s/n, 10003 Cáceres, Spain

Wężyk 2018; Li et al. 2017; Nizami et al. 2017; Rodriguez-Veiga et al. 2017).

Remote sensing techniques have been used to map land cover and land use worldwide. Many studies have addressed land cover from a general standpoint (Ahmed et al. 2015; Akike and Samanta 2016; Bolton et al. 2018; Qi et al. 2014; Zhao et al. 2016; Zhou et al. 2014) and others have focused on the study of a specific vegetation stratum. In the later studies, vegetation is typically divided into two strata: the overstory and the understory strata. The overstory is the highest vegetation level, which corresponds to the tree canopies. Many studies have focused on this stratum, particularly by characterizing forest structure, tree cover density, or tree species (Dalponte et al. 2012, 2014; Ferreira et al. 2016; Ghosh et al. 2014; Kim et al. 2011). The understory is the lowest level and includes shrubs and pasture. However, although this stratum plays a key role in forest ecosystems (Tuanmu et al. 2010), there are far fewer studies focusing on the understory than those addressing the overstory. Nonetheless, some works such as those by Magiera et al. (2016), Stavrakoudis et al. (2014), and van Lier et al. (2009) have focused on the mapping of understory habitats from remote sensing data. Additionally, several studies have focused on the detection of invasive shrubs (Malahlela et al. 2015; Müllerová et al. 2013; Niphadkar et al. 2017) and others have analyzed the relationship between low strata and the overstory, as well as the influence of shrubs on the reflectance of higher-level canopies (Eriksson et al. 2006; Landry et al. 2018; Tuanmu et al. 2010).

As shown in Fassnacht et al. (2016), the different remote sensing techniques used in vegetation cover analyses utilize either passive (multispectral or hyperspectral images) or active (SAR and LiDAR data) optical data, or a combination of both. However, our study focused on passive optical data-based analyses, which require the spectral and spatial resolutions[1] to be considered in order to render accurate maps. In the case of passive remote sensing, whether its main sources are satellites or aerial platforms, the spectral resolution decreases when the spatial resolution increases (Dalponte et al. 2009). The spectral resolution in these types of sensors ranges from the visible (VIS), near-infrared (NIR), and shortwave-infrared (SWIR) of the electromagnetic spectrum. On the other hand, the spatial resolution ranges from coarse with a pixel size of more than 250 m (CSR), medium with a pixel size of 30 m (MSR), high with a pixel size of 10 m (HSR), very-high with a pixel size ranging from 1 m to 5 m (VHRS), and ultra-high with a pixel size of 1 m or less (UHSR).

Therefore, multispectral sensors can be classified into three groups depending on pixel size. The first group consists of MSR- or HSR-resolution approaches such as of Landsat-8, SPOT, and Sentinel-2 satellite imagery. The second group is comprised of high-resolution technologies such as GeoEye, Pleiades, IKONO, QuickBird, RapidEye, and WorldView, all of which achieve a VHSR resolution. See Table 1 for more details.

UHSR-resolution approaches typically involve aerial imagery with a spatial resolution of < 1 m, ranging from 0.25 to 0.50 m, such as those implemented by the National Plan of Aerial Orthophotography (PNOA) in Spain. The PNOA imagery provides a continuous coverage throughout the Spanish territory, with a spectral resolution of 4 bands including the VIS and NIR with an update period of 2 or 3 years, depending on the area.

The selection of a particular remote sensing sensor depends on the aim of the study. For instance, Landsat imagery is commonly used to map land cover from a general standpoint and when a long time series is needed, given that this technology possesses the longest time series capacity available (Ahmed et al. 2015; Bolton et al. 2018; Zhao et al. 2016; Zhou et al. 2014). In recent years, Sentinel-2 imagery has been proven as a viable alternative to Landsat, and many studies have adopted said technology for land cover mapping in forested areas (Fragoso-Campón et al. 2019; Godinho et al. 2017; Immitzer et al. 2016; Mura et al. 2018; Nomura and Mitchard 2018).

Additionally, spatial resolution plays a key role in heterogeneous landscapes due to the confusion between discrete and continuous cover types (Adam et al. 2014). In this regard, as mentioned by Ferreira et al. (2016), the differences in the spectral variability within species are significantly lower than the spectral variability among species. The potential of VHSR imagery has been demonstrated in vegetation species mapping in several ecosystems. For instance, heterogeneous coastal landscapes have been assessed with RapidEye (Adam et al. 2014), tree species discrimination with GeoEye, Pleiades, and WorldView2 (Fang et al. 2018), other applications with IKONOS (Kim et al. 2011), tree species crown mapping in African savannas with QuickBird (Boggs 2010), or a combination between VHSR and hyperspectral or LiDAR in the Southern Alps (Dalponte et al. 2012), Boreal forests (Dalponte et al. 2014), and tropical seasonal semi-deciduous forests (Ferreira et al. 2016). Regarding the study of the understory vegetation with VHSR, RapidEye was used to analyze the reflectance signatures of shrub species in the Caucasus (Magiera et al. 2016), whereas QuickBird and an EO-1 Hyperion (Stavrakoudis et al. 2014) or IKONOS were used in the study of ericaceous shrubs (van Lier et al. 2009). Fewer studies have employed UHSR imagery for vegetation mapping. One example is a study by Müllerová et al. (2013), which focused on the detection of an invasive species in the Czech Republic using RapidEye technology

[1] Please note that temporal resolution was not analyzed in this work.

Table 1 Main characteristics of multispectral sensors

Group[1]	Satellite[2]	Spatial Resolution	Number of Bands	Spectral bands[3]	Spectral range	Available[4]
MSR	Landsat-8	30 m	9	VIS–NIR-SWIR	15 nm to 180 nm	–
HSR	SPOT	10 m	5	VIS–NIR	70 nm to 170 nm.	–
	Sentinel-2	10 m	12	VIS–NIR-SWIR	15 nm to 180 nm	–
VHSR	GeoEye	2 m (PA 0.5 m)	5	PA-VIS–NIR	35 nm to 140 nm	€
	IKONO	4 m (PA 1 m)	5	PA-VIS–NIR	66 nm to 96 nm	€
	QuickBird	2.5-2.9 m (PA 0.6-0.9 m)	5	PA-VIS–NIR	60 nm to 140 nm	€
	RapidEye	6.5 m	5	VIS-RE-NIR	55 nm to 90 nm	€
	WorldView	2 m (PA 0.5 m)	8	VIS-RE-NIR1-NIR2	40 nm to 180 nm	€

[1]*MSR* medium spatial resolution, *HSR* high spatial resolution, *VHSR* very-high spatial resolution

[2]Satellite Data from Labrador García et al. (2012)

[3]*PA* panchromatic

VIS red-blue-green

RE red edge

NIR near-infrared

SWIR shortwave-infrared

[4](–) available for free; (€) available under request and fee payment

and a historical UHSR series. One more example, is the study by Wang et al. (2019) which used UHSR images to classify woody and herbaceous vegetation in a dryland ecosystem in China. Another study estimated tree crown delineation and tree cover from UHSR imagery obtained from the PNOA (Borlaf-Mena et al. 2019; Cantero Fauquier et al. 2017). Moreover, some studies (e.g., Riaño et al. (2007)) have used UHSR images to study the fuel-type map of a predominantly shrub-land area in central Portugal in conjunction with LiDAR data. Table 2 summarizes the main characteristics of these previous studies.

As previously mentioned, although these techniques have been proven to be effective in mapping vegetation species throughout various ecosystems, only a few studies have focused on *dehesa* landscapes. The *dehesa* is a Mediterranean agro-silvo-pastoral system that covers more than 3 million hectares in the Iberian Peninsula (Caballero Díaz et al. 2015; Diaz et al. 1997). There are many ways to define the *dehesa*. From an economic standpoint, Olea and San Miguel-Ayanz (2006) described it as "*an agrosilvopastoral system developed on poor or non-agricultural land and aimed at extensive livestock raising.*" Diaz et al. (1997) proposed another definition based on a landscape standpoint: "*Dehesas are pasturelands populated by holm (Quercus ilex) and/or cork (Quercus suber) oaks, with an understory of open grassland, cereal crops, or Mediterranean scrub.*" As described by Olea et al. (2005), the *dehesa* is located in the southern region of the Iberian Peninsula, both in Spain and Portugal, where it is locally referred to as "*montado*", mainly in *Extremadura* (Spain), *Alentejo* (Portugal), and *Andalucía* (Spain), with extensions of approximately 12 500, 8000, and 7000 km^2, respectively. The *dehesa* not only plays a key role in the rural economy, as they are a source of cork, acorns, natural pastures, aromatic and medicinal plants, honey, and mushrooms (Canteiro et al. 2011), but also in preserving the ecosystem biodiversity, as they are the main feeding areas of a large number of endangered bird species, and also host a large number of wintering birds from northern Europe (Diaz et al. 1997).

In the *dehesa* environment, the spatial distribution of the vegetation cover plays a crucial role in the productivity of pastures and tree growth, and therefore many studies have focused on the relationship between them. However, characterizing the positive or negative relationship between understory and overstory species remains a challenge because different studies often reach conflicting conclusions. For example, Rivest et al. (2011) analyzed the effect of shrub encroachment on pasture yield, holm oak *(Quercus ilex)* growth, and acorn production, and concluded that encroachment affected pasture and tree production in Mediterranean *dehesa*s in a species- and climate-dependent manner. Other authors have analyzed how shrubs benefit tree recruitment. In this sense, Pulido et al. (2010) concluded that shrubs protect acorns and provide shadow, thereby allowing for better seedling establishment. An alternative point of view is the relationship between soil organic matter (i.e., a universal soil quality and land degradation indicator) and vegetation cover, studied by Pulido-Fernández et al. (2013). This study demonstrated that soil organic carbon stocks were closely related to the tree density and shrub cover, although further analysis is

Table 2 Overview of studies using very high spatial resolution images for land cover mapping

Study	Overstory/ Understory	Satellite/sensor	Spectral resolution[1]	Spatial resolution	Classification Algorithm[2]	Predictors	Pixel/ object based	Accuracy assessment	Overall accuracy
Adam et al. (2014)	O/U**(not shrub)	Multispectral (RapidEye imagery)	5 bands (440–850 nm)	5 m	SVM, RF	Spectral Bands	Pixel	Error Matrix and McNemar's test	93.07% (RF); 91.80% (SVM); Z = 1.96
Boggs, 2010	O	SPOT-5 and QuickBird	SPOT-5 (G-R-NIR) QuickBird (VNIR)	10 m (SPOT-5) and 0.6 m (QuickBird pan-sharpened)	Pixel threshold NDVI value and OBIA techniques	Spectral bands, VI and texture (OBIA)	Object	Error Matrix	85–97% (QuickBird); 53–81% (SPOT-5)
Eroğlu et al. (2010)	O/U	IKONOS	4 bands (VNIR)	4 bands (4 m) and 1 panchromatic band (1 m)	Parallelepiped non-parametric rule	Spectral Bands	Pixel	Error Matrix	82.5%
Burnett et al. (2019)	O/U	WorldView2	WorldView2 (VNIR + Y+RE + NIR2)	2 m and 0.5 m (pan-sharpened)	RF	Spectral bands and texture features	Pixel	Error Matrix	97%
Dalponte et al. (2012)	O	VHR multispectral (GeoEye-1 satellite); VHR hyperspectral images (AISA Eagle sensor); LiDAR data	H: 126 bands (402.9–989.1 nm); M: 4 bands (450–920 nm) and panchromatic; LiDAR HR 8.6 points per m^2 LR 0.48 points per m^2)	All datasets: 1 m	SVM, RF	Spectral Bands, LiDAR metrics	Pixel	Error Matrix	H + LiDAR: 74.1–83% (SVM); 70.8–80% (RF) M + LiDAR: 64.8–75.3% (SVM); 63.1–70.6% (RF)
Dalponte et al. (2014)	O	Hyperspectral (aerial) and LiDAR	160 bands (410–990 nm) LiDAR 7.4 echoes per m^2	0.40 m	SVM	Spectral bands	Pixel	K-fold cross validation	85.4–93.5%
Fang et al. (2018)	O	GeoEye, Pleiades, and WorldView2	GeoEye (VNIR), Pleiades (VNIR) and WorldView2 (VNIR + Y+RE + NIR2) LiDAR 6.6 points per m^2	2 m multispectral (MS) bands, as well as an approximately 0.5 m panchromatic band; LiDAR 0.5 m	RF	Spectral bands, vegetation indices, and Texture	Object	Error Matrix	62%
Ferreira et al. (2016)	O	Hyperspectral (aerial) and multispectral (Wordview-3)	260 bands (VNIR 450–970 nm; SWIR 970–2400 nm)	1.0 m H - 5.0 WV3	Lda, RBF-SVM, RF	Spectral bands, vegetation indices	Pixel	Error Matrix	70% (VNIR); 75% (VNIR + VI); 84% (VNIR-SWIR); 57.4% (WV-3 VNIR); 74.8% (WV-3 VNIR + SWIR)

Table 2 (continued)

Study	Overstory/ Understory	Satellite/sensor	Spectral resolution[1]	Spatial resolution	Classification Algorithm[2]	Predictors	Pixel/ object based	Accuracy assessment	Overall accuracy
Ghosh et al. (2014)	O	Hyperspectral: Two airborne (HyMAP) and one space-borne (Hyperion) and LiDAR	Hympa 125 bands (450–2480 nm); Hyperion 146 bands (400–2500 nm); LiDAR 12 points per m^2	4 m, 8 m, and 30 m	SVM, RF	Spectral bands, Minimum Noise Fraction, vegetation indices (86 hympa and 84 hyperion)	Pixel	Error Matrix and McNemar's test	70–85%
Kim et al. (2011)	O	IKONOS	4 bands (VNIR)	4 bands (4 m) and 1 panchromatic band (1 m)	MLC	Spectral Bands	Pixel & Object	Error Matrix	63.9% (PBC); 76.8% (SBC)
Magiera et al. (2016)	U	RapidEye & simulated satellite bands (IKONOS, Quickbird2, World-View2)	4 bands (VNIR)	RapidEye (5 × 5 m)	–	Spectral Bands	–	The Jeffries-Matusita distance (JMD) as a separation measure	–
Malahlela et al. (2015)	U	WorldView2	WorldView2 (VNIR + Y+RE + NIR2)	2 m	Logistic regression	Spectral bands, vegetation indices and geographical data (DEM, Aspect)	Pixel	Error Matrix and ROC (AUC)	87%
Müllerová et al. (2013)	U	Aerial photographs, multispectral and RapidEye	Aerial (Panchromatic); Multispectral & RapidEye (VNIR)	0.5 (Aerial, multispectral); 2 m (RapidEye)	MLH (pixel) and C (Object-based)	Spectral bands and texture (OBIA)	Pixel Vs Object	Error Matrix	In terms of user's accuracy (UA), producer's accuracy (PA), quantity disagreement (QD), and allocation disagreement (AD)
Niphadkar et al. (2017)	U	GeoEye and WorldView2	GeoEye (VNIR) and WorldView2 (VNIR + Y+RE + NIR2)	2 m	MLH (pixel) and NNC (Object based)	Spectral bands and vegetation indices	Pixel Vs Object	Error Matrix	60%
Stavrakoudis et al. (2014)	O/U	QuickBird and an EO-1 Hyperion	QuickBird (VNIR); 155 bands Hyperion (VNIR + SWIR)	QuickBird (2.4 m); Hyperion (30 m)	SVM	Spectral bands	Pixel	Error Matrix	67.58% (QuickBird); 77.21% (Fusion)
van Lier et al. (2009)	U	IKONOS and Landsat_TM	4 bands (VNIR)	3 m (IKONOS) 30 m (Landsat)	NNC	Spectral bands and vegetation indices (NDVI and TCC)	Object	Error Matrix	70–80% (VHR); 71–78% (Landsat)

Table 2 (continued)

Study	Overstory/ Understory	Satellite/sensor	Spectral resolution[1]	Spatial resolution	Classification Algorithm[2]	Predictors	Pixel/ object based	Accuracy assessment	Overall accuracy
Wang et al. (2019)	O/U	Aerial photograph	3 bands (RGB)	0.10 m	CART, SMV, RF, GBDT	Spectral bands and derived color space	Pixel	Error Matrix	77.7% (CART); 76.9% (SMV); 78.1% (RF); 80.2% (GBDT)

[1] *VIS* Red (G)–Blue (B)–Green (G)

RE red edge

NIR near-infrared

VNIR red-blue-green-near-infrared

SWIR shortwave-infrared

[2] If multiple algorithms were used, the best was underlined

CART classification and regression tree

C combination of automated hierarchical, iterative, and ruled-based classification

GBDT gradient boosting decision tree

LDA linear discriminant analysis

MLH maximum likelihood classifier

NNC nearest neighbor classification

RBF-SVM support vector machine—radial basis function

RF random forest

SVM support vector machine

required. In another study, Santos-Silva et al. (2011) demonstrated that the tree canopy cover factor in *montados* was highly related with the macrofungal richness and sporocarp production, which highlighted the need for new management strategies to preserve *montados* with a canopy cover of 30–50%. Godinho et al. (2016b) investigated the influence of the environment, land management, and spatial factors on recent *montado* changes in Portugal, their results indicated that most of the variance in the large-scale distribution of recent *montado* loss was due to land management practices associated with grazing intensity and type, as well as shrub control techniques. Lastly, Godinho et al. (2016a) found that there was a significant statistical relationship between tree canopy cover factors in *montado* ecosystems and land surface albedo and temperature, and discussed how these two biogeophysical parameters are related with climate change, specifically in increasingly arid ecosystems. In this sense, the water balance is also related to the vegetation cover and affects several factors such as evapotranspiration, runoff, interflow, and infiltration (Becker et al. 2019; Dias et al. 2015; Dionizio and Costa 2019). Current approaches in hydrological calibration are based on spatially distributed models that require remote sensing data as input (Athira et al. 2016; Becker et al. 2019; Chen et al. 2019b). Therefore, it is necessary to know the spatial distribution of several parameters such as topography, soil and land cover characteristics, and meteorological details. Thus, knowing the spatial distribution of vegetation cover is essential to assess complex hydrological models, given that the vegetation cover factor reduces runoff and enhances infiltration, thereby increasing groundwater recharge (Netzer et al. 2019).

Despite the importance of having maps that accurately characterize the vegetation of the *dehesa*s ecosystem for hydrological modeling, water balance models, and management strategies of the regions in question, only a few studies have examined the *dehesa* vegetation using remote sensing techniques. Among these studies, we found a few that used MSR images such as Landsat (Carreiras et al. 2006; Godinho et al. 2016a) and HSR images of Sentinel imagery (Fragoso-Campón et al. 2019; Godinho et al. 2017). Moreover, hardly any researchers have used VHSR or UHSR in *dehesa*s ecosystems, most of which have focused on the overstory stratum. For instance, Castillejo-González et al. (2010) applied QuickBird VHR images to obtain the tree canopy cover factor in a *dehesa* environment. Moreover, Cantero Fauquier et al. (2017) and Borlaf-Mena et al. (2019) mapped the tree crown shape of a *dehesa* environment using a segmentation approach with PNOA UHSR images, covering only three spectral bands (RBG) coupled with LiDAR data. Similarly, Lavado Contador et al. (2012) analyzed the temporal dynamics of the tree canopy cover factor in a *dehesa* ecosystem using PNOA UHSR images, also only covering three spectral bands (RBG). From a water balance standpoint, few studies have focused on the hydrological processes of *dehesa* environments. These studies include some of the earliest reports (Ceballos and Schnabel 1998; Cerda et al. 1998; Joffre and Rambal 1993), as well as more recent studies focused on soil water balance based on MODIS NDVI products (Campos et al. 2013, 2016). However, further research is needed to characterize hydrological processes in *dehesa* environments via spatially distributed models, where access to accurate vegetation spatial patterns is mandatory. Hence, this study attempted to go further by applying the current remote sensing techniques to render high accurate ad hoc land cover maps. Notably, the categories should be related to the potential runoff generation capability. Thus, it is applicable to hydrological modeling and, the precision is improved if compared to other global land cover database.

Therefore, our study sought to develop a methodology to characterize vegetation in a *dehesa* environment using PNOA UHSR imagery for future use in hydrological modeling. The specific goals of this study were: (1) to obtain customized high-resolution maps of the vegetation in both the overstory and understory strata; (2) to develop a method to reduce field campaigns by transferring the information of the training dataset to different images for which ground data extraction was not necessarily performed; (3) to identify vegetation types based on ecosystem management approaches and runoff generation capability; (4) to evaluate the influence of the spatial resolution of land cover maps on potential runoff estimation in a *dehesa* environment.

2 Materials

2.1 Study area

The study area corresponds to a *dehesa* environment in the Extremadura region in Spain. The area limits correspond with the two neighboring watersheds of the *Tamuja* and *Aljucén* rivers, which are approximately 458 and 253 km^2 respectively, and extends between latitudes 39° 00′–39° 30′ N and longitudes of 6° 21′–5° 54′ W (Fig. 1). Based on the Worldwide Bioclimatic Classification System (Rivas-Martinez and Rivas-Saenz 1996–2019), the area corresponds to the Mediterranean West Iberian biogeographic region (15a: Luso-Extremaduran), the Mediterranean pluviseasonal continental variant, and the mesomediterranean thermoclimatic belt. The overstory vegetation is mainly comprised of holm oaks (*Quercus rotundifolia*), although sparse areas of cork oaks (*Quercus suber*) and pyrenean oaks (*Quercus pyrenaica*) can also be found. The

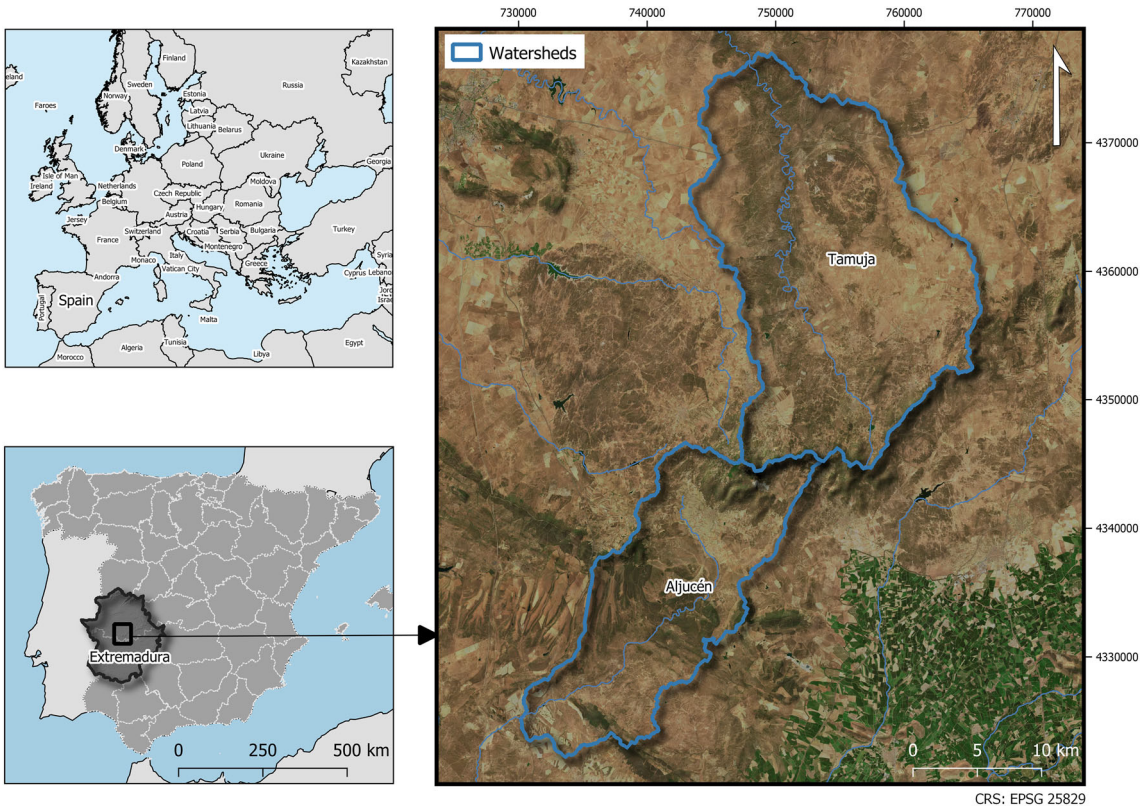

Fig. 1 Study area

understory is more diverse and several evergreen shrub species are distributed in the study area. The main species in the *dehesa*s ecosystem are *Cistus ladanifer*, *Retama sphaerocarpa, Lavandula stoechas, Thymus mastichina, Genista hirsute, Phillyrea angustifolia, Erica arborea*, *and Erica australis* (Devesa Alcaraz 1995). The herbaceous vegetation is predominantly acidophilus pasture, which is characteristically ephemeral and with low coverage and spring phenology, followed lastly by dry agricultural areas (i.e., small grain, meadow, or forage lands for grazing). Finally, other non-vegetation land covers such as rocky outcrops, small cattle ponds, and impervious surfaces (e.g., roads or roofs of rural houses) are also present in the study area, albeit with a much lower occurrence.

2.2 Imagery dataset

The UHSR imagery used in this study was obtained from the PNOA (Ministerio de Fomento 2019). As previously mentioned, the PNOA imagery has the great advantage of providing continuous coverage throughout the Spanish territory. The images analyzed in this study were taken with a 4-band multispectral sensor (visible and NIR) at a 0.25-m spatial resolution in June of 2016. The images are typically used as a cartographic background in numerous fields, including civil and forestry engineering, and as a basis for the photointerpretation of different surface elements (primarily in the combination of RGB bands) and to update the Spanish Land Occupation Information System (SIOSE) (Vila-García et al. 2015). Hernández-López et al. (2013) discussed the importance of the spectral information provided by PNOA images for applications related to the extraction of physical parameters, the evolution of forest cover, and agronomic analysis of plant species. However, few studies have taken advantage of the spectral information of the bands beyond their use as a cartographic background. Otherwise, only the visible spectrum (RGB) is typically used (Borlaf-Mena et al. 2019; Lavado Contador et al. 2012). This is probably due to the fact that RGB information can be downloaded for free from the National Geographic Institute's Download Center (IGN), whereas the NIR data is only available upon request.

In the study area, a total of twenty-five images were selected for the analysis, which represent the entire variability of the *dehesa* environment (Fig. 3). The pre-processing of the PNOA images is described in the metadata of the imagery and includes the following steps: mosaic making, radiometric correction, enhancement, and cutting of images with coating. The images are supplied in a 1:5000 tile and two products are available in parallel: one was made in the visible spectrum (RGB) and another in false infrared color (NIR-R-G), in this case, the metadata

indicated that the infrared layer was not radiometrically corrected.

2.3 Field data

The field data in the *Tamuja* and *Aljucén* watersheds were randomly selected by visual interpretation of the UHSR images representing the wide range of cover types in the *dehesa*. As reported by Ferreira et al. (2016), only areas that were clearly distinguished by visual interpretation were drawn, thus ensuring the spectral responses of all the species considered in the analysis. Moreover, a field campaign was designed for the identification of ambiguous cases as proposed in Mas et al. (2010). As a result, the field dataset covered approximately 1.8 million pixels (Fig. 2). Thus, the land cover classes in the *dehesa* environment were grouped into two levels of disaggregation, as shown in Table 3. On the one hand, the class-level, in which different classes within the species were defined, focused on the discrimination of understory strata. On the other hand, the different species in the *dehesa* environment were grouped in the macro-class level. This classification also fits a similar hydrologic response following the criteria of the National Engineering Handbook (NRCS 2009), and thus the different classes and macro-classes considered herein can be grouped according to their runoff generation capacity (Table 3).

2.4 Image pre-processing and predictors

A multiband raster stack was created for each image to account for the four spectral bands (i.e., NIR, red, green, and blue) in the analysis. Similar to previous studies (see Table 2), additional features (i.e., in addition to the spectral information) were used as predictors to improve the discrimination of the vegetation. These predictors included vegetation indices (VI), soil indices (SI), and textural features (TF). The PNOA imagery had an 8-bit color depth, and thus the pixel values ranged from 0 to 255. Therefore, similar to the method proposed by Borlaf-Mena et al. (2019), the digital numbers were first normalized from 0 to 1 using Eq. (1).

$$\mathrm{NIR_n} = \frac{\mathrm{NIR}}{255}; \quad \mathrm{Red_n} = \frac{\mathrm{Red}}{255}; \quad \mathrm{Green_n} = \frac{\mathrm{Green}}{255}; \quad \mathrm{Blue_n} = \frac{\mathrm{Blue}}{255} \tag{1}$$

where NIR, Red, Green, and Blue are the digital values of the pixel in each band, and $\mathrm{NIR_n}$, $\mathrm{Red_n}$, $\mathrm{Green_n}$, and $\mathrm{Blue_n}$ are the normalized values of the pixels.

The VI, SI, and TF analysis was conducted using the Sentinel Application Platform (SNAP) software developed by the European Space Agency (ESA). The well-known normalized difference vegetation index (NDVI) is by far the most widely used index among the VI; however, other indices have also been proven to be useful (Fang et al. 2018; Ferreira et al. 2016). Due to the low spectral resolution of the PNOA imagery, only a limited number of indices can be computed with the available bands. Table 4 summarizes the indices considered in this study.

Regarding the use of SI, the most common indices are the Brightness Index (BI) and the Color Index (CI) (Escadafal 1993), and although they are not fully implemented in vegetation classifications (Fragoso-Campón et al. 2019), they have been proven to be useful as they can improve the discrimination between low green vegetation canopy covers and bare soil (Huete and Post 1984; Richardson and Wiegand 1977).

Regarding the TF, the grey-level co-occurrence matrices (GLCM) (Haralick and Shanmugam 1973) is a widely used method to compute textures metrics. As reported by Burnett et al. (2019), the texture metrics can be computed from a combination of bands or the principal component, but it is also possible to achieve good results using only a single band. In this case, we used only the NIR band to compute the derived textured measures due to the spatial resolution of the images and to the specific importance of this band in the vegetation response. As recommended by Hall-Beyer (2017), the descriptive statistics (mean and variance) of the GLCM texture measurements were applied. Specifically, means were utilized for classification and the variance was included as additional information, as these parameters were not expected to be highly correlated (Hall-Beyer 2017). The analysis was performed for all angles via

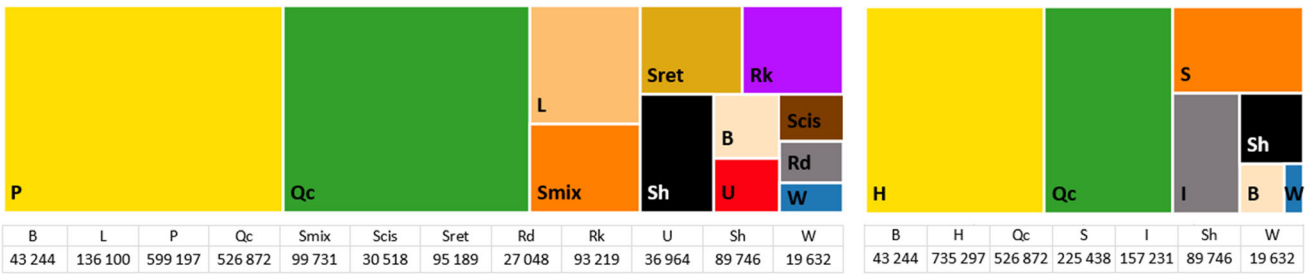

B	L	P	Qc	Smix	Scis	Sret	Rd	Rk	U	Sh	W
43 244	136 100	599 197	526 872	99 731	30 518	95 189	27 048	93 219	36 964	89 746	19 632

B	H	Qc	S	I	Sh	W
43 244	735 297	526 872	225 438	157 231	89 746	19 632

Fig. 2 Field dataset pixels grouped according to both levels of disaggregation considered **a** class level; **b** macro-class level

Table 3 Land cover types analyzed

Stratum	Land cover type	Class-level categories	Runoff generation	Macro-class-level categories
Overstory	Holm Oaks (*Quercus rotundifolia)*	Qc		Quercus (Qc)
	Cork oaks (*Quercus suber)*			
	Pyrenean oaks (*Quercus pyrenaica*)			
Understory	Mixed shrubs *(Lavandula stoechas, Thymus mastichina, Genista hirsute, Phillyrea angustifolia, Erica arborea and Erica australis)*	Smix		Shrub (S)
	Retama sphaerocarpa	Sret		
	Cistus ladanifer	Scis		
	Pasture	P		Herbaceous plants (H)
	Dry agricultural land	L		
Non-vegetation	Bare soil	B		B
	Roads	Rd		Impervious (I)
	Rocky outcrops	Rk		
	Roofs of rural houses	U		
	Shadows	Sh	-	Sh
	Waterbodies	W	-	W
Capacity for run off generation legend:	 very high	 high	 medium	 low

probabilistic quantization, using a pixel displacement of 4 and a 7 × 7 window size.

2.5 Training and Validation Groups

Two different groups of PNOA images of the study area were considered in the analysis: the training group and the validation group (Fig. 3). The training group was used to train the model, whereas the validation group was used to perform an independent accuracy verification to evaluate the capability of the classifier to be used in neighboring images that were not used to train the model. The statistical analyses were performed with the R statistical computing software (R-Core-Team 2018).

First, a seventeen-image training group was used to obtain a training dataset. For each image, a different region

Table 4 Vegetation, water, and soil indices considered in this study

Type	Index	Equation*	Reference
Vegetation	NDVI	$NDVI = \frac{\mathrm{NIR}_n - \mathrm{Red}_n}{\mathrm{NIR}_n + \mathrm{Red}_n}$ (2)	Rouse Jr et al. (1974)
	SAVI**	$SAVI = (1+L)\cdot\frac{\mathrm{NIR}_n - \mathrm{Red}_n}{(\mathrm{NIR}_n + \mathrm{Red}_n + L)}$ (3)	Huete (1988)
	MSAVI2	$MSAVI2 = \frac{1}{2}\cdot\left[(2\cdot(\mathrm{NIR}_n + 1) - \sqrt{(2\mathrm{NIR}_n + 1)^2 - 8(\mathrm{NIR}_n - Red_n)}\right]$ (4)	Qi et al. (1994)
Water	NDWI	$NDWI = \frac{\mathrm{Green}_n - \mathrm{NIR}_n}{\mathrm{Green}_n + \mathrm{NIR}_n}$ (5)	Gao (1996)
Soil	BI	$BI = \sqrt{\frac{Red_n^2 + Green_n^2}{2}}$ (6)	Mathieu et al. (1998)
	CI	$CI = \frac{\mathrm{Red}_n - \mathrm{Green}_n}{\mathrm{Red}_n + \mathrm{Green}_n}$ (7)	Escadafal and Huete (1991)

*Adaptation of the traditional formulation to the normalized values of the bands

**L = 0.50

NDVI (Normalized Difference Vegetation Index); SAVI (Soil Adjusted Vegetation Index); MSAVI2 (Second Modified Soil Adjusted Vegetation Index), NDWI (Normalized Difference Water Index); BI (Brightness Index); CI (Color Index)

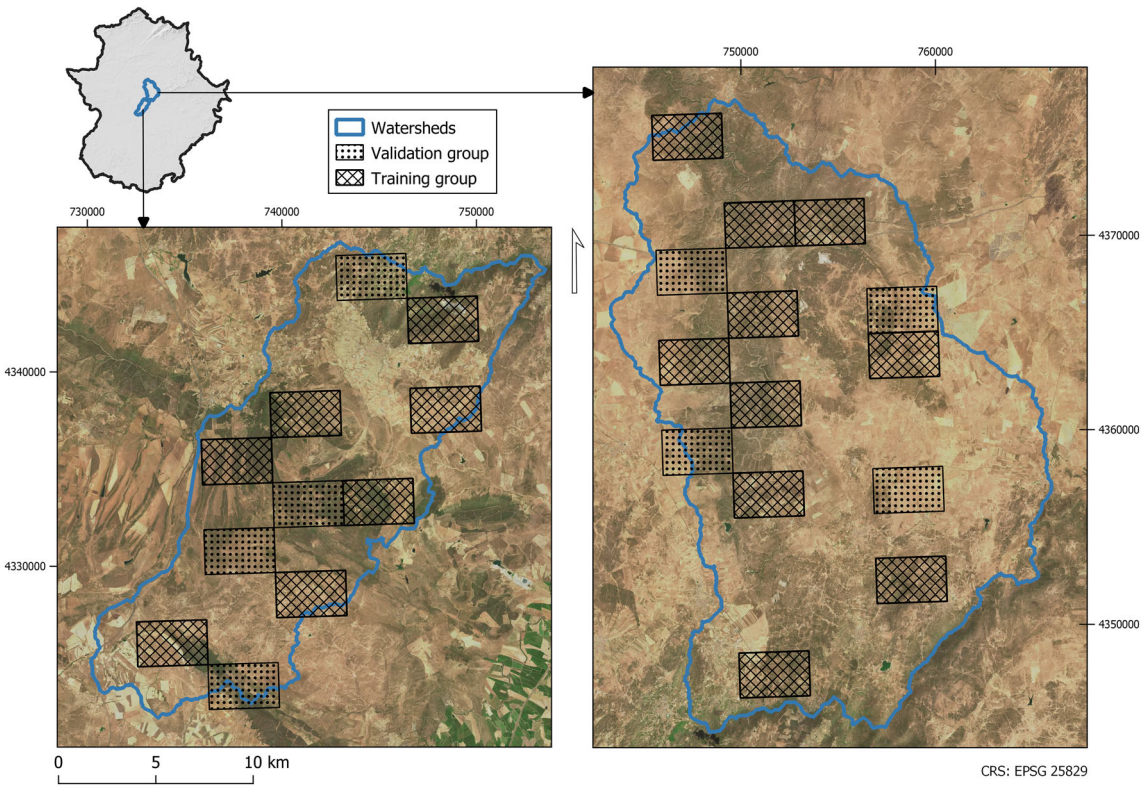

Fig. 3 Images of the PNOA tile used for training and validation

of interest (ROI) dataset was randomly geolocalized, representing all the land cover types in each tile. Then, the values of the predictors in each category were obtained using the *raster R package* (Hijmans 2019). Afterward, all the ROI datasets were merged into one, representing all the ROI of the training group. At this point, the training dataset was randomly divided into two groups ensuring to maintain the class balance: ROI Dataset 1 and ROI Dataset 2 (complete data sets in Rdata format are provided in Online Resource 1). The separability of the classes and macro-classes was tested based on the spectral response, VI, SI, and TF using the Jeffries-Matusita distance (JMD) for

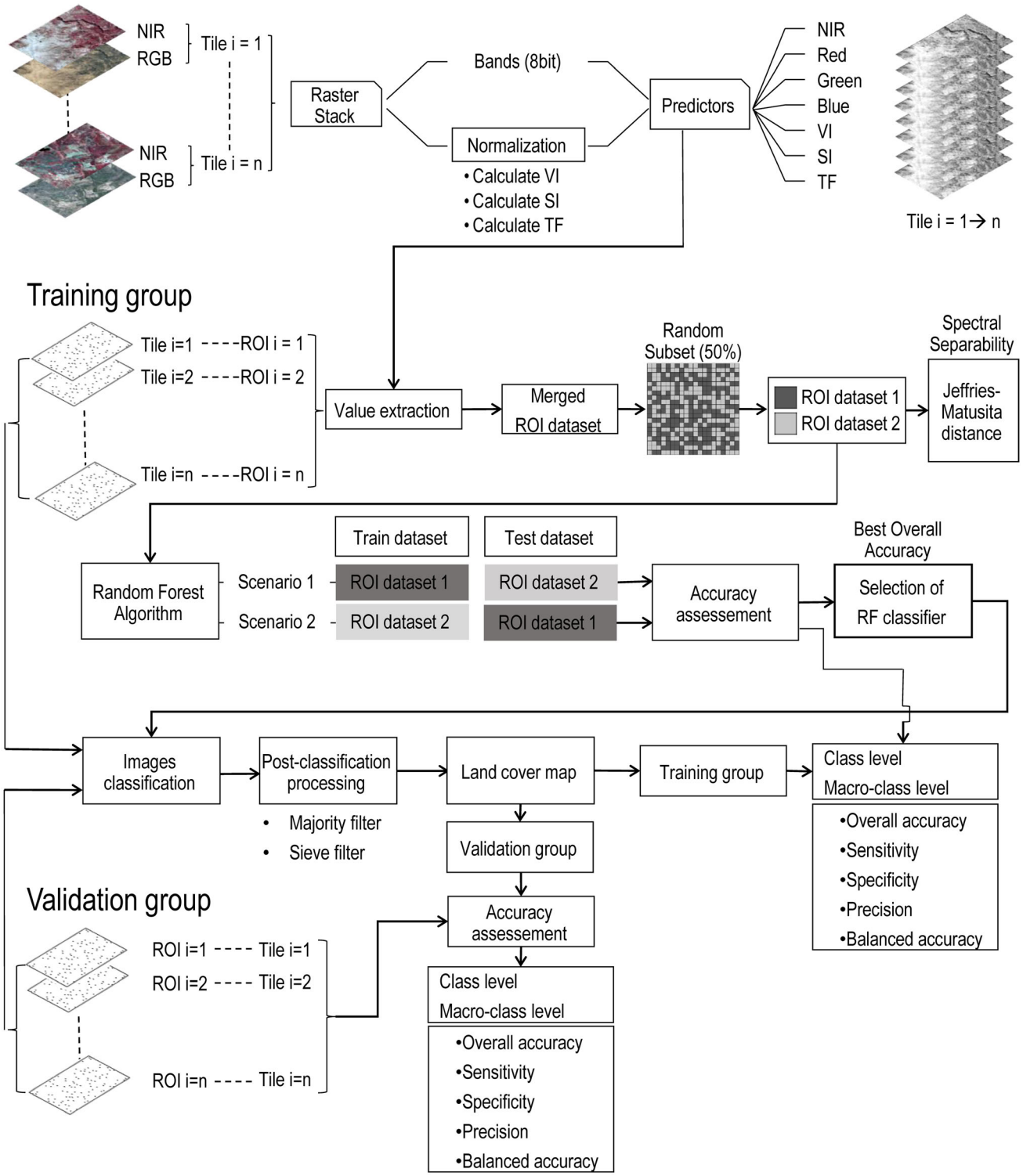

Fig. 4 UHSR imagery processing flowchart proposed in this study

multiclass cases via the *varSel R package* (Dalponte and Ørka 2016). The JMD measures the separability among categories based on the information that each predictor can provide to the analysis. As shown in Lasaponara and Lanorte (2007b), the JMD bounds are between 0 and 1.41 (asymptotic to the value 2), whereby higher values indicate

Table 5 Accuracy measures in each category based on error matrix information

Metric	Definition	Equation
Sensitivity	Proportion of predictions that are accurately classified as positive in each category. Also called producer's accuracy	$\text{Sensitivity} = \frac{TP}{TP+FN}$ (8)
Specificity	Proportion of predictions that are accurately classified as negative	$\text{Specificity} = \frac{TN}{TN+FP}$ (9)
Precision	Proportion of the reference area included accurately in each category to which it belongs. Also called user's accuracy	$\text{Precision} = \frac{TP}{TP+FP}$ (10)
Balanced accuracy	The average proportion of predictions accurately classified, considering both the TP and TN possibilities	$BA = \frac{1}{2} \cdot (sensivity + specificity)$ (11)

TP True Positive

FN False Negative

FP False Positive

TN True Negative

higher separability. JMD values below a threshold value of 1 are generally assumed to represent poor separability. Therefore, the separability of the proposed categories was verified using a JMD threshold of 1.

Secondly, an eight-image validation group was used to obtain the validation dataset. Following the procedure explained above, ROIs of each image were randomly geolocalized to represent the land cover in each tile.

2.6 Classification technique

When the input predictors for the classification are obtained from a mixed origin (spectra, indices, and textures), non-parametric machine learning methods such as the random forest (RF) (Breiman 2001) and the support vector machine classifier (SVM) have been proven effective in previous studies (Fassnacht et al. 2016). As shown in Table 2, both algorithms have been widely used in previous studies and are well documented (Ghosh et al. 2014).

In this study, a pixel-level supervised classification was conducted using RF, as this approach is more time-efficient. Thus, the classifications were performed using the *RandomForest R package* (Liaw and Wiener 2002). The RF classifier was trained considering two scenarios as shown in Fig. 4. Both training datasets, ROI Dataset 1 and ROI Dataset 2, were use twice (i.e., as training data or as independent test data each time). Finally, the RF classifier with the best performance in terms of overall accuracy was selected for the classification. The analysis was conducted for both the class and macro-class levels.

Two parameters had to be configured to train the RF classifier: the number of decision trees (Ntree), which was set to 500, and the number of variables to be selected and tested to achieve an optimal split when growing the trees (Mtry). In each scenario, the best Mtry values were trained before the classifier was defined.

2.7 Post-classification processing

When applying a pixel-level classification approach to an image with high spatial resolution, it is assumed that salt-and-pepper noise will occur. There are some techniques to reduce this noise in the final classification (Kim et al. 2011) and one of them is related to a classification post-process that improves the accuracy of the final maps (Stavrakoudis et al. 2014; Su 2016). In this work, the classified images were smoothed using the majority filtering and sieving methods (Mas et al. 2010). The filtering process was carried out with algorithms implemented in the QGIS software. First, the *SAGA majority filter* (Conrad 2010) was applied, considering a square search mode with a radius of 2. Afterward, the *GDAL sieve filter* (GDAL-documentation 2019), which removes groups of raster pixels smaller than a provided threshold size (in pixels), was set to a threshold value of 10 to replace the pixels with the pixel value of the largest neighboring pixels values.

2.8 Accuracy assessment

The accuracy measures used herein were based on error matrix information, which allows to obtain derived metrics to evaluate the performance of the RF (Congalton and Green 2008). The error matrices were performed with the *caret R package* (Kuhn et al. 2018). First, we considered an overall accuracy (OA) parameter, which represents the global ratio of correct predictions considering all the categories on the map. Additionally, the error matrix provides other information to test each category. Therefore, the metrics used for the accuracy assessment by categories (considering the class or macro-class level) were defined

Table 6 NRCS runoff curve number (CN)

UHSR imagery				Corine land cover		
Class-level categories	NRCS land cover	Hydrologic condition	CN[1]	CLC-18	Description	CN[2]
Qc	Woods	Good	55	111	Continuous urban fabric	98
Smix	Range-Brush	Fair	56	131	Mineral extraction sites	85
Sret	Range-Brush	Poor	67	211	Non-irrigated arable land	75
Scis	Range-Brush	Good	48	223	Olive groves	64
P	Herbaceous vegetation	Fair	69	231	Pastures	61
L	Close-seeded	Good	72	242	Complex cultivation patterns	64
B	Gravel roads	–	85	243	Land principally occupied by agriculture, with significant areas of natural vegetation	77
Rd	Paved roads	–	98	244	Agro-forestry areas	69
Rk	Impervious		98	311	Broad-leaved forest	52
U	Impervious		98	313	Mixed forest	52
Sh	It is asummed that the shadow comprises the pasture around trees	–	69	321	Natural grasslands	69
W	–	–	100	323	Sclerophyllous vegetation	68
				324	Transitional woodland-shrub	60
				333	Sparsely vegetated areas	78

[1]Source: Table 9.1 and 9.5 in (NRCS 2004)

[2]Source: Table 2.3 in Ministerio de Fomento (2016) using the equation CN = 5080/(P_o + 50.8)

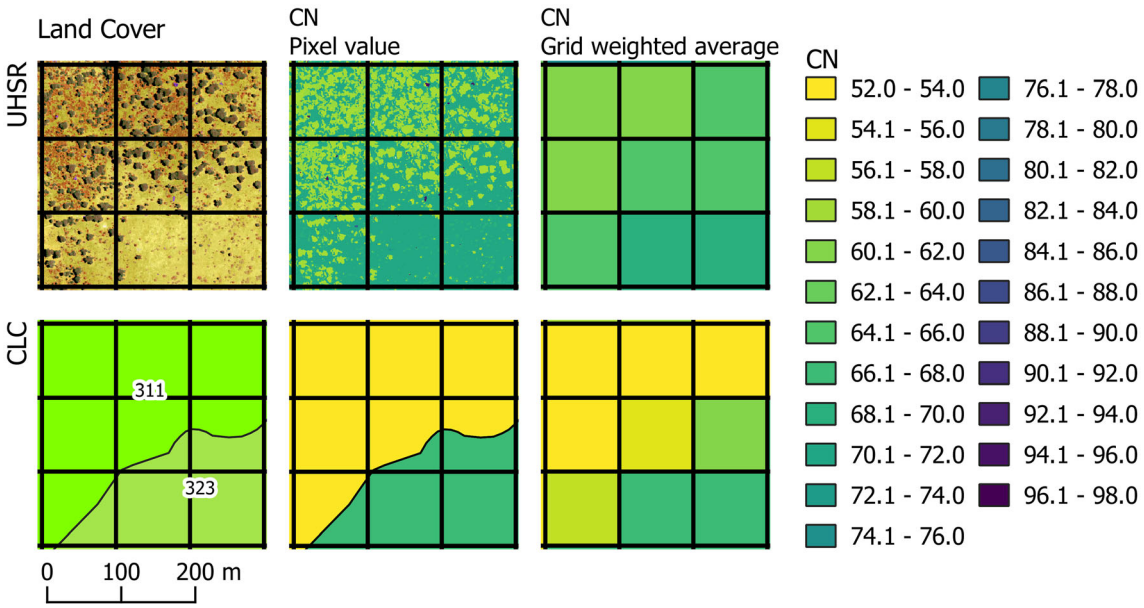

Fig. 5 Example of the grid cell weighted average CN values

based on the procedures described by Franklin (2010), as summarized in Table 5.

As shown in Fig. 4, the accuracy evaluations were carried out in two phases. First, the best RF classifier in the training group was analyzed by comparing the OA in the two considered scenarios. Then, once the RF classifier with the best performance was selected, the accuracy metrics in each category were obtained for both class and macro-class analyses. Afterward, the capability of the RF classifier to be used in other validation group images that were not used to train the model was evaluated. Therefore, a zonal histogram of the ROI over the post-processed classified

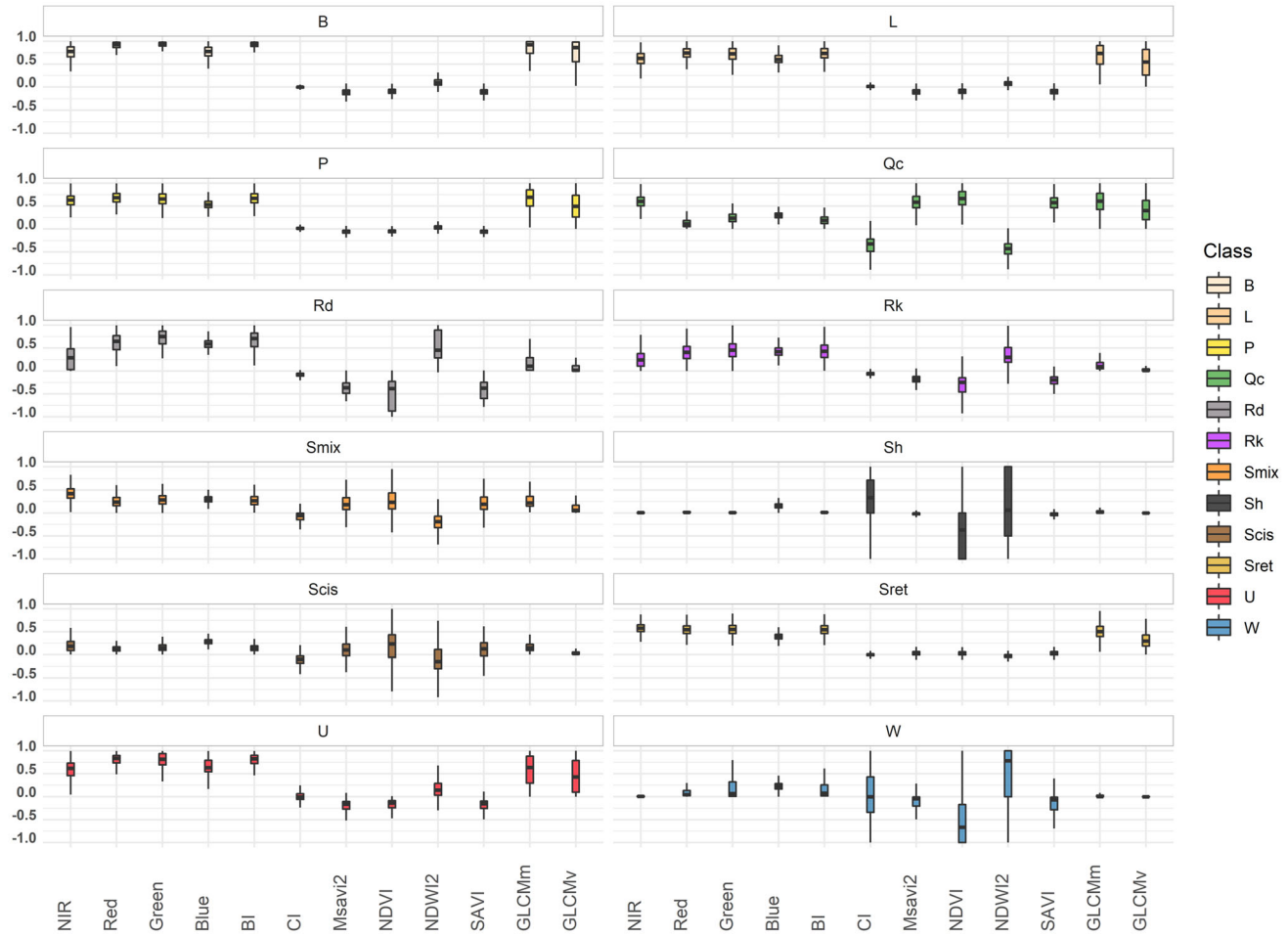

Fig. 6 Class-level feature characterization. The values of optical bands (NIR, red, green, and blue) and textures (GLCMm and GLCMv) are displayed as normalized values from 0 to 1

images was obtained for each tile, after which the information was merged to calculate a global error matrix of the validation group. In this case, the accuracy was based on polygons as sampling units (Congalton and Green 2008).

2.9 Influence of the spatial resolution of land cover maps on runoff

The hydrologic response was evaluated following the National Resources Conservation Service Curve Number method[2] (NRCS-CN) (NRCS 2009), where the runoff volume is calculated following Eq. (12).

$$Q = \frac{(P - 0.2S)^2}{P + 0.8S} \tag{12}$$

where Q is the surface runoff, P is the total rainfall and S is the potential maximum retention.

The S factor, which is measured in mm, is computed from the main factor of the method, the dimensionless curve number (CN) parameter following Eq. (13)

$$S = \frac{25400}{CN} - 254 \tag{13}$$

Subsequently, the CN refers to the potential runoff capability of a complex area, whereby the higher CN value indicates a higher potential runoff capability. Therefore, based on the criteria of the National Engineering Handbook, the CN depends on cover (land cover and treatment class) and soil type.The main limitation of the NRCS-CN is the soil initial antecedent moisture before the rainfall-runoff process begins (Durán-Barroso et al. 2016) and in this study an average condition was considered.

In this work, the influence of the spatial resolution of the land cover maps on runoff was conducted by comparing

[2] It was not until 1994 that the Soil Conservation Service (SCS) changed its name to the National Resources Conservation Service (NRCS), so the methodology is also known as the SCS-CN method.

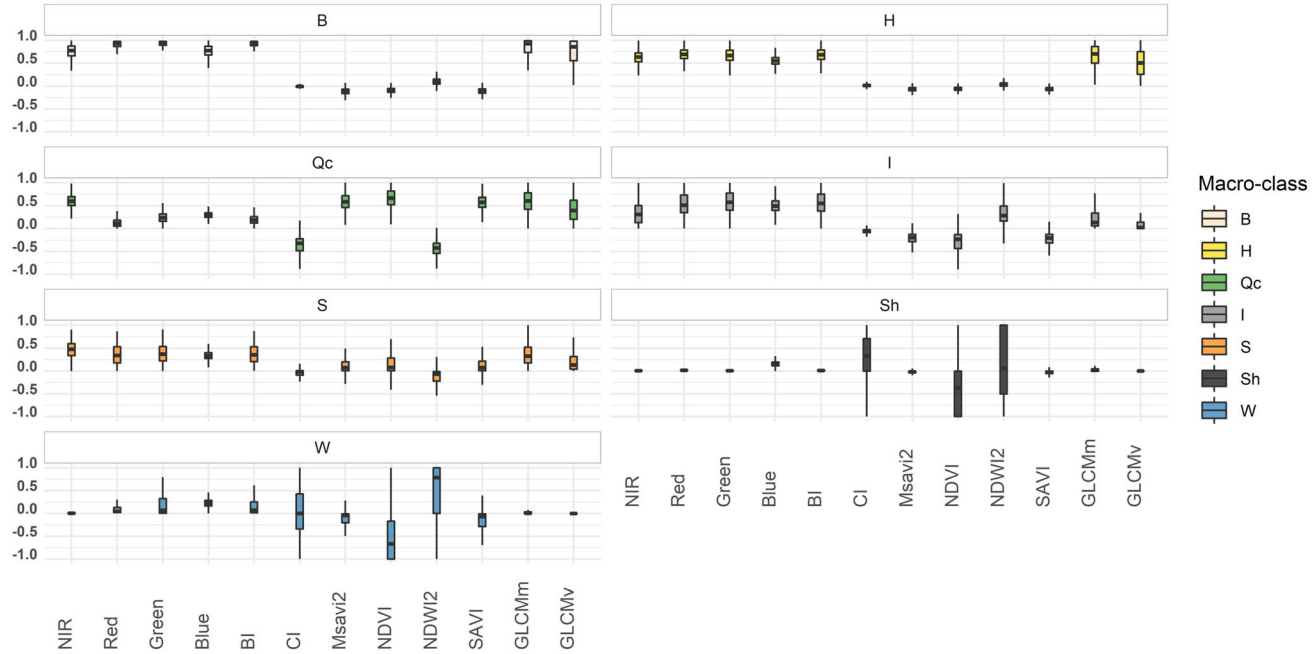

Fig. 7 Macro-class-level features characterization at (MC). The values of optical bands (NIR, red, green, and blue) and textures (GLCMm and GLCMv) are displayed as normalized values from 0 to 1

the CN values derived from the UHRS land cover maps with the CN values derived from the Corine Land Cover (CLC). CLC is a land cover database frequently used in Europe for hydrologic purpose (Petroselli and Grimaldi 2018; Psomiadis et al. 2020; Walega and Salata 2019) and, the version published in 2018 was used.

In the case of the UHSR land cover, given that the land cover was in fact grouped into categories depending on their hydrologic response, it is possible to obtain the CN values directly from the lookup tables of the National Engineering Handbook (NRCS 2004) and, the class-level categories were used with this aim (Table 6). However, the CLC database, only provides general information of covertures. That is why, hydrological interpretation was needed and, the lookup table proposed in Spain by Ministerio de Fomento (2016) was used in terms of CN values. Finally, the soil group was chosen following the results in Ferrer i Juliá (2003) resulting in a soil group type B throughout the study area (Fragoso et al. 2017).

In order to compare the differences in the estimation of CN values, the weighted average CN values derived from both data sources were computed using a grid with a cell size of 100 × 100 m (Fig. 5), following Eq. (14)

$$CN_{grid} = \sum_{i=1}^{n} \frac{CN_i \cdot A_i}{A} \tag{14}$$

where, CN_i is the CN value in the ith land cover portion within the grid cell, A_i is the ith area of land cover portion, n is the total number of differences land covers portions in the grid cell and A is the total area of the grid cell. Consequently, in each grid cell, there was a pair of averaged CN values, corresponding to each land cover data sources: the UHSR-CN and the CLC-CN.

Therefore, the analysis of the effect of land cover spatial resolution on the CN value, was conducted using the mean absolute difference (MAD) and the global root mean square difference (RMSD). The MAD measures the difference between the values in each grid cell expressing the comparisons of CLC-CN versus UHSR-CN. Therefore, it can be summarized if the disagreement between each pair means overestimation or underestimation of the CN value. The RMSD measures the difference between both land cover datasets in the estimation of the CN values. The MAD was computed for each CLC-CN value following Eq. (15), and the RMSD for the global dataset following Eq. (16)

$$MAD_{CN} = \frac{1}{N}\left(\sum_{i=1}^{N}\left(CN_{grid.CLC} - CN_{grid.UHSR}\right)_i\right) \tag{15}$$

$$RMSD = \sqrt{\frac{1}{N}\left(\sum_{i=1}^{N}\left(CN_{grid.CLC} - CN_{grid.UHSR}\right)_i^2\right)} \tag{16}$$

where, $CN_{grid.CLC}$ is the weighted average CLC-CN value in the i^{th} grid cell, $CN_{grid.UHSR}$ is the weighted average

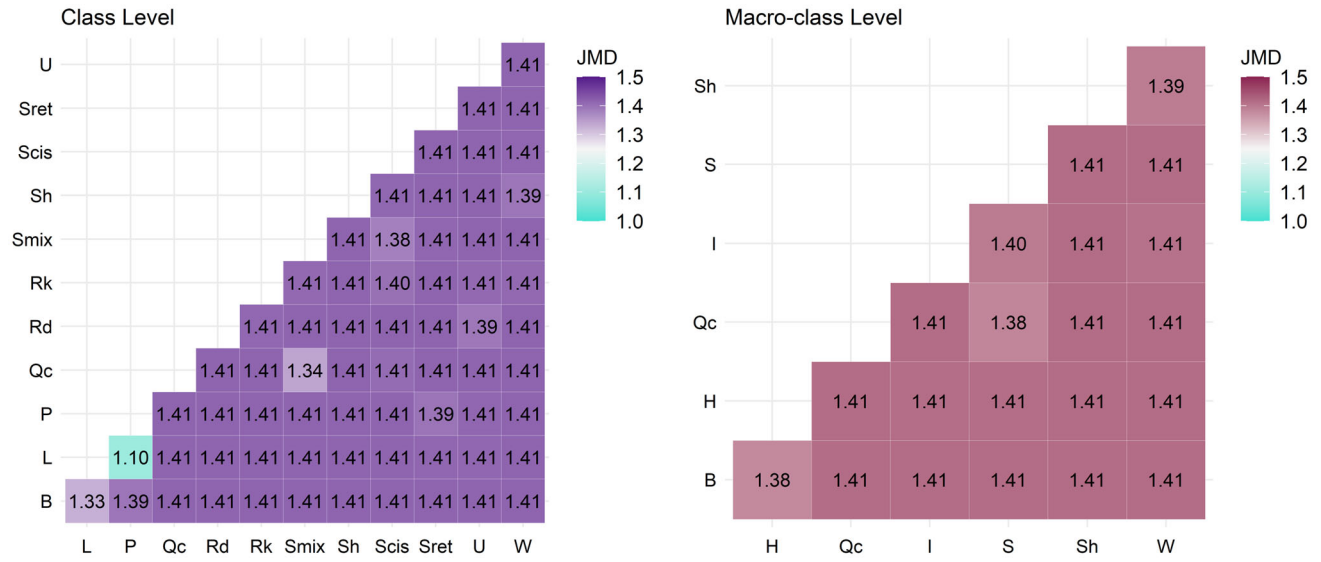

Fig. 8 Jeffries-Matusita distance (JMD) between the categories in both levels of disaggregation: class and macro-class

Table 7 Overall accuracies (OA) and kappa indices obtained from the error matrices in both considered scenarios

			Class level		Macro-class level	
Scenario	Training	Test	OA (%)	Kappa	OA (%)	Kappa
1	ROI Dataset 1	ROI Dataset 2	91.6	0.8922	95.8	0.9412
2	ROI Dataset 2	ROI Dataset 1	91.5	0.8915	95.7	0.9407

UHSR-CN value in the ith grid cell and, N is the number of grid cells with the same $CN_{grid.CLC}$.

3 Results

3.1 Feature characterization

The feature characterization was inspired by a spectral signature of the categories. Due to the low spectral resolution of PNOA images, our approach considered not only the spectral information of the bands but also the information of all the predictors. Therefore, the characterization was based on a box-plot graph representing the values of the predictors from the first quartile to the third quartile, which is referred to as the interquartile range (IQR). The analysis shows different responses among the categories at the class (Fig. 6) and macro-class (Fig. 7) levels.

The overstory stratum that represents the holm oaks presented high differences between the normalized optical bands, and presented the highest values in NIR band. In contrast, the red, green, and blue bands had much lower values, with an IQR below 0.20 in all cases, particularly the IQR of the blue band, with a value of 0.09. Regarding the indices, it is worth noting that holm oaks exhibit higher negative values in CI and NDWI2, but present higher positive mean values in terms of NDVI, second modified soil adjusted vegetation index (MSAVI2), and soil adjusted vegetation index (SAVI). The holm oaks also have a high response in terms of texture in both the GLCMm and GLCMv predictors.

The understory stratum categories presented different responses among categories at the macro-class level, which discriminated between shrubs and herbaceous plants. The shrub stratum also presented different responses within categories at the class level. However, in this case, herbaceous plant categories did not present significant differences at the class level. Therefore, understory categories exhibited a similar magnitude in all the optical bands, and no significant differences were observed compared to the overstory observations. Moreover, the values were lower for shrubs and higher for herbaceous plant categories. It is worth noting that, in this case, the blue band also presented a low IQR value of approximately 0.13 in both understory strata. Furthermore, when considering shrub species, Sret presented the highest values in all optical bands, whereas Scis had the lowest values. The IQR of the blue band was also very narrow, ranging from 0.8 to

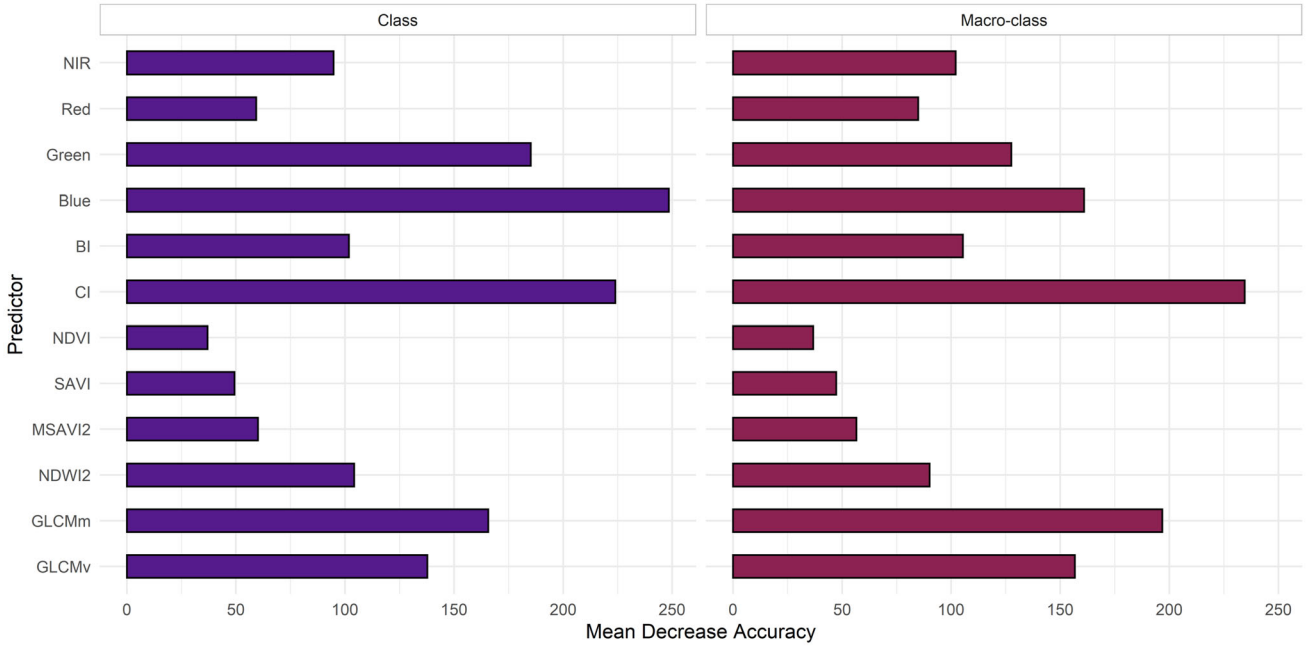

Fig. 9 Predictor importance in the RF algorithm based on mean decrease accuracy at the class and macro-class level

Fig. 10 Class- and macro-class-level predictor importance across categories in the RF algorithm

Table 8 Overall accuracies (OA) and kappa indices obtained

	Class level		Macro-class level	
Group	OA (%)	Kappa	OA (%)	Kappa
Training	91.6	0.89	95.8	0.94
Validation	78.3	0.74	86.3	0.82

0.10. Regarding the indices, the CI in the understory stratum was close to zero in all the categories, showing similar responses among and within species. When evaluating the VI, shrubs exhibited low values, showing different responses within species: the lowest values were observed for Sret and the highest values for Smix. The herbaceous stratum had negative VI values with a narrow IQR of 0.06, showing similar responses within species. The understory stratum presented different responses in terms of texture features. Particularly, while herbaceous plants had higher GLCMm and GLCMv predictor values (similar to the overstory stratum), the shrub stratum presented lower values and different responses within species, with Sret exhibiting the highest values. The lowest values were observed for Scis, which also had a narrow IQR.

Finally, the non-vegetation categories exhibited different responses at the macro-class level, distinguishing between impervious surface categories at class-level. First, related to the optical response, B presented the highest values of all bands, indicating that the IQR value of the green band in this category was very narrow, with a value of only 0.08. Additionally, impervious surfaces exhibited lower values in the NIR band; however, Sh and W

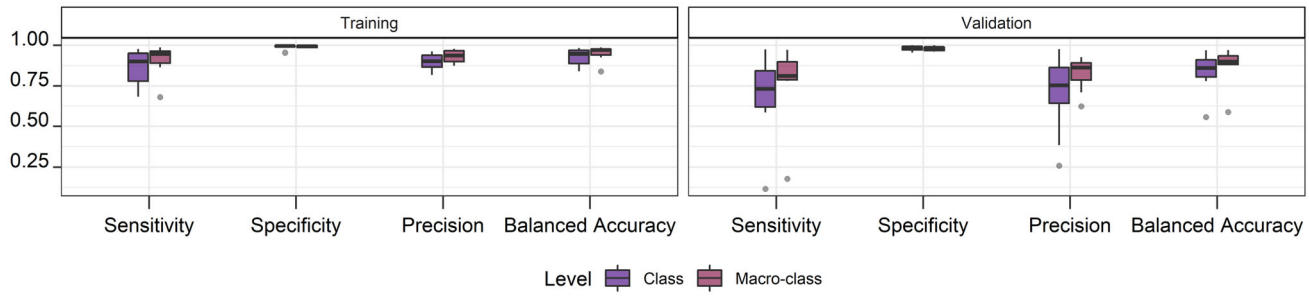

Fig. 11 Summary of the random forest classifier error matrix results

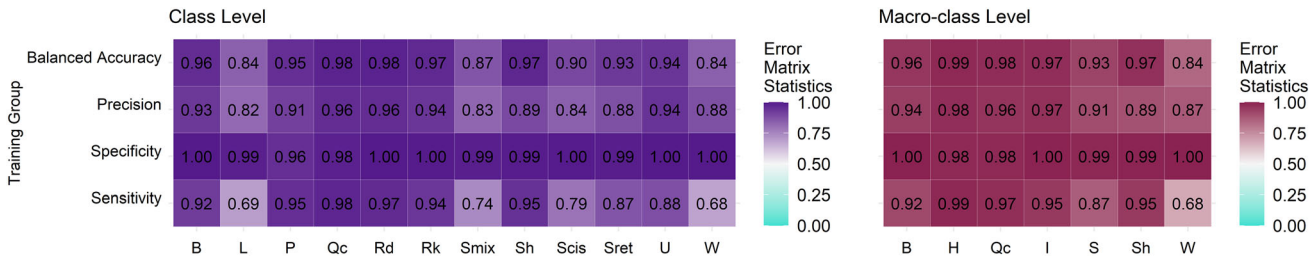

Fig. 12 Error matrix statistics of the training group random forest classifier

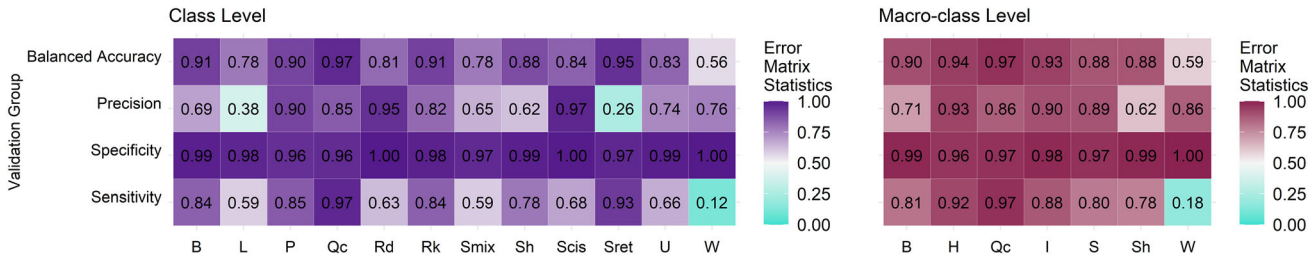

Fig. 13 Error matrix statistics of the random forest classifier in the validation group

presented by far the lowest values in all optical bands. Regarding the indices, impervious surfaces exhibited a CI value close to zero, with a narrow IQR but with similar responses within species. For this index, Sh and W exhibited high IQR values of over 0.70. Regarding the BI, the highest values were observed for B and U, which also had narrow IQR values of 0.017 and 0.09, respectively. Sh exhibited by far the lowest BI value, with a narrow IQR of 0.013. Concerning the NDWI2, not only did the highest values were observed for impervious surfaces and W, but the IQR values for Sh and W were also wider, with values higher than 1. Finally, in terms of texture, impervious categories presented low values except for U, which had higher values in terms of both mean and IQR (> 0.5). The Sh and W classifications exhibited by far the lowest mean TF values, as well as a narrow IQR value of less than 0.04.

The JMD showed a good spectral separation between the categories at both levels of disaggregation (Fig. 8). In the class-level analysis, the values ranged from 1.10 to 1.41. The lowest values occurred within the classes of the herbaceous macro-class. Specifically, P and L resulted in a JMD of 1.10. When considering the macro-class level, the highest JMD values remained at 1.41. However, the lowest values improved for the H and B pair, as well as the S and Qc pair, which achieved a JMD of 1.38.

3.2 Selection of the random forest classifier

As previously mentioned, the RF classifier was trained in two scenarios (Fig. 4) using the training dataset twice (i.e., each time either as a training or test set). The OAs achieved for each run are summarized in Table 7, and demonstrate the robustness of our developed classifier, with an OA and kappa index of over 91% in both instances. The results in scenario 1 were slightly better, and thus the RF classifier obtained in scenario 1 was selected for image classification.

Regarding the importance of the predictors, Fig. 9 shows the mean decrease in the predictive accuracy of the RF algorithm in Scenario 1. The RF algorithm uses the out of bag (OOB) samples that were not used to build the trees to measure the prediction capacity of each predictor. As explained in Hastie et al. (2009), when a tree is grown, OOB samples are used to measure the accuracy of the prediction. Then, each predictor is permuted in the OOB samples and the accuracy is calculated again. Afterward, the decrease in accuracy is averaged over all trees for each predictor. Higher values suggest a more important role of the predictor in the classification process.

CI, the blue band, GLCMm, and GLCMv were found to be the most important classification predictors, followed by other less important but also strong predictors, such as the green band, BI, and the NIR band. VI had the least importance, according to our analysis.

Additionally, the importance of each predictor varied across the categories, as illustrated in Fig. 10. The blue band became notably important to classify shrub species. Moreover, the most important predictors for herbaceous category classification were CI and GLCMm. Finally, CI was the most valuable predictor for impervious surfaces.

3.3 Accuracy assessment

As indicated by Table 8, the RF algorithm delivered accurate results. The OA values were higher for the macro-class level than for the class level analysis, and the results in the validation group were lower than those of the

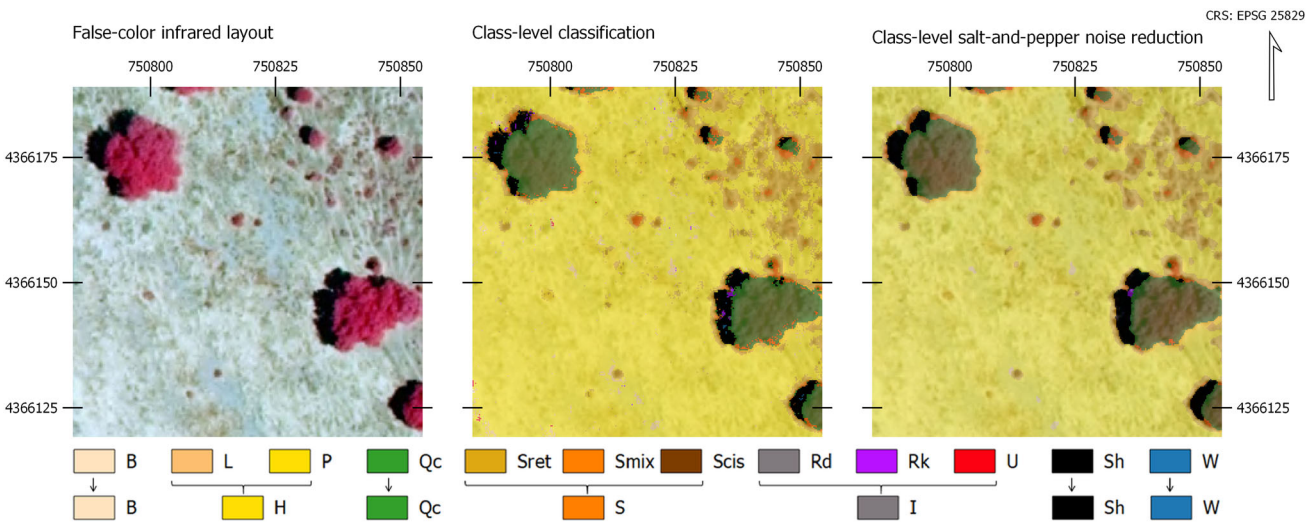

Fig. 14 Salt-and-pepper noise reduction post-classification processing results

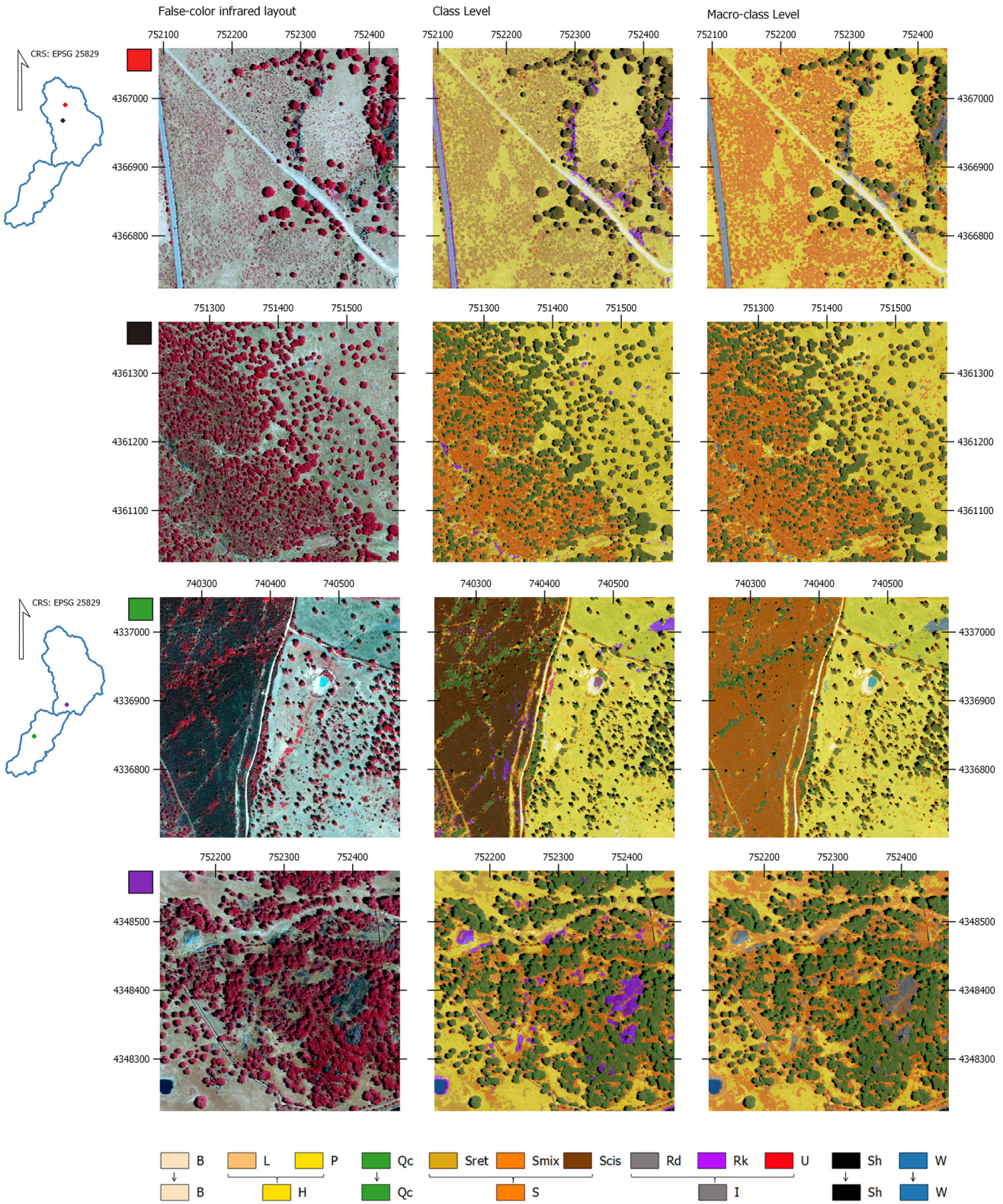

Fig. 15 Land cover maps of the *dehesa* environment

training group. However, despite these differences, the overall performance of our classifier was still outstanding.

The error matrices obtained herein are supplied as supplementary material for both groups. The matrices are

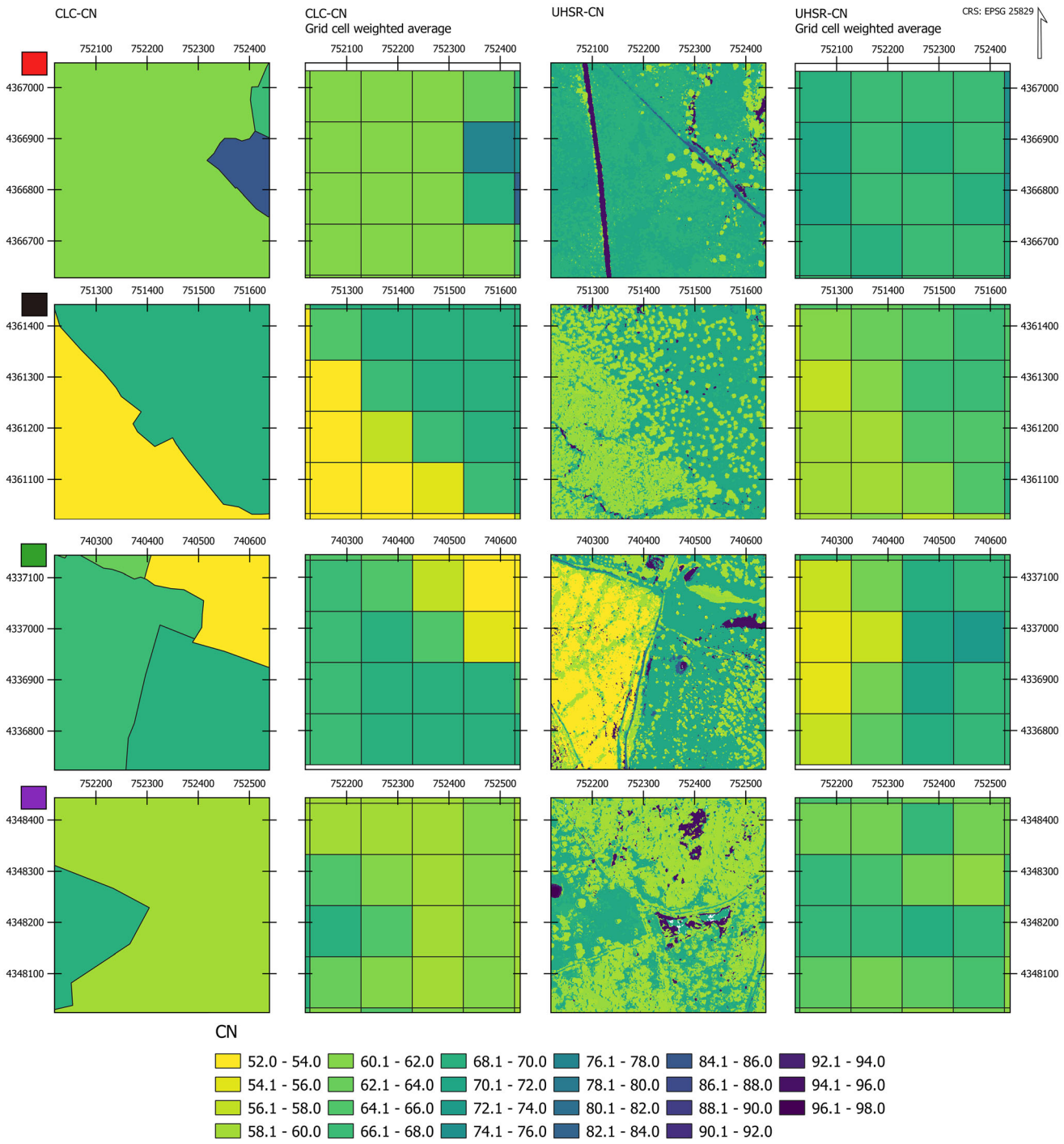

Fig. 16 Grid cell weighted average CN values derived from the UHSR land cover maps (UHSR-CN) and the CLC (CLC-CN) in a the *dehesa* environment

expressed in terms of pixel count and percent of prediction for each category.[3]

Overall, the training group rendered more accurate results than the validation group, based on the error matrix data (Fig. 11).

When considering vegetation cover, the training group Qc classification (Fig. 12) achieved excellent results, with a sensitivity, specificity, and balanced accuracy of 0.98. Moreover, at the macro-class level, excellent results were

[3] Online Resource 2: see Tables S1 and S2 for more details on the training group at the class level. For the macro-class-level analysis, see Tables S3 and S4. For the validation group at class level, see Tables S5 and S6. For the analysis at the macro-class level, see Tables S7 and S8.

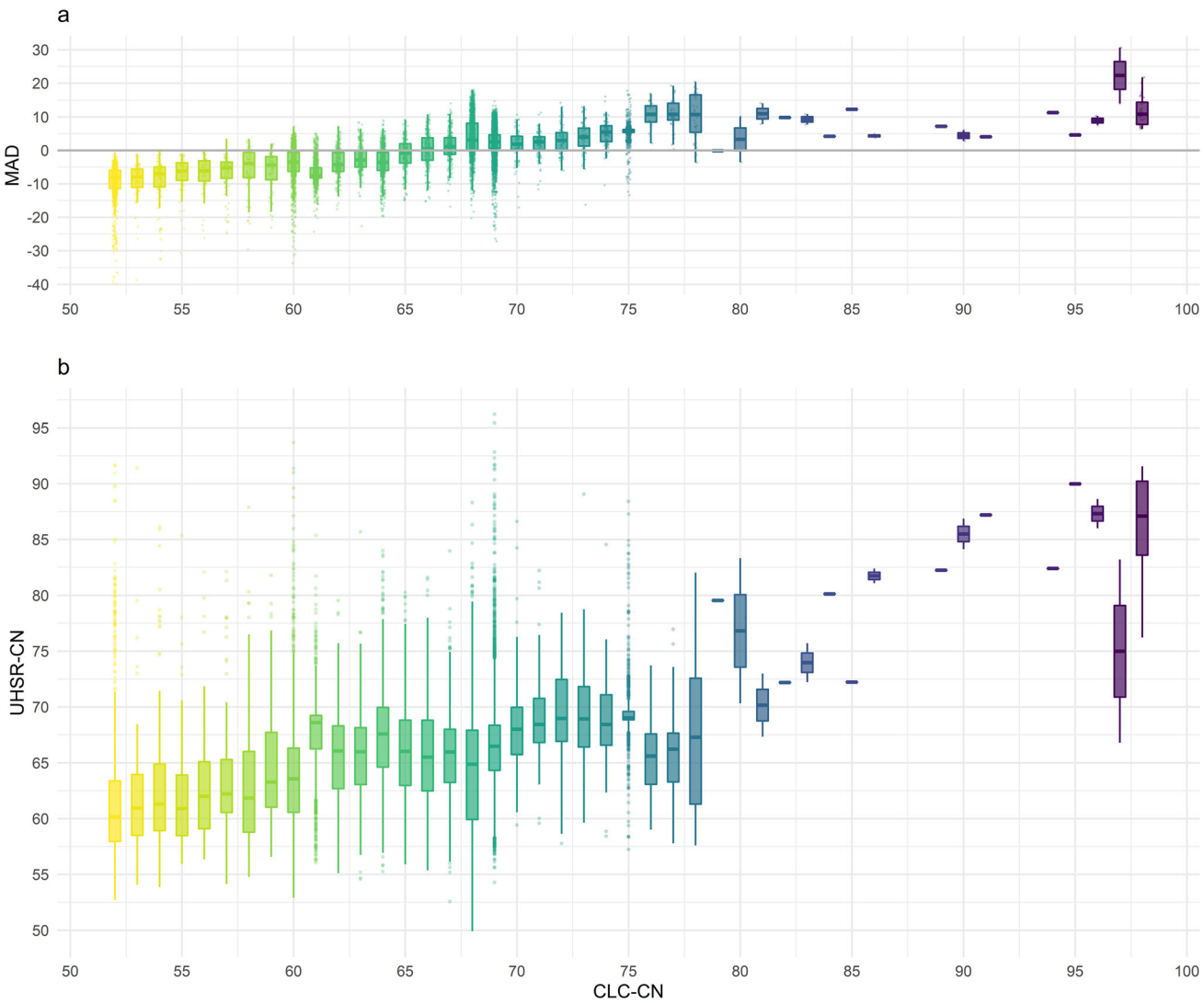

Fig. 17 Influence of the spatial resolution of the land cover maps in the CN comparing the grid cell weighted average CLC-CN value versus UHSR-CN values **a** mean absolute difference (MAD), **b** box-plot of CLC-CN values versus UHSR-CN values

achieved for the shrub stratum, showing a sensitivity of 0.80, a specificity of 0.97, and a balanced accuracy of 0.88. When considering the class-level disaggregation, the best results were observed for Sret, followed by Scis and Smix. Regarding the herbaceous stratum, the results were excellent at the macro-class level. However, at the class level, the statistics for the L class were poorer than those for P class. Specifically, L exhibited balanced accuracy and sensitivity values of 0.84 and 0.69, respectively, whereas P reached a 0.95 value for both parameters. Considering the non-vegetation covers, the results were excellent for B and I. Good results were also obtained when considering the class level disaggregation in Rk, Rd, and U. However, the values obtained for W were less accurate, with a sensitivity of 0.68 and a balance accuracy of 0.84.

In terms of balanced accuracy, the results in the validation group (Fig. 13) showed values ranging from 0.56 to 0.97 at the class level and from 0.59 to 0.97 at the macro-class level. As previously mentioned, the accuracy values were lower than those for the training group, especially at the class level, where significant decreases in sensitivity and precision were observed. However, vegetation classifications remained accurate for Qc, H, and S. In contrast, a decrease in accuracy was observed for non-vegetation classes such as Sh, with W having the worst classification performance.

3.4 Land cover results

Figure 14 illustrates how the images were smoothed using the majority filtering and sieving methods to reduce salt-

and-pepper noise. Figure 15 illustrates the representative land cover types of the *dehesa* environment upon the application of post-classification processing. The final land cover maps for all the images of the training group are shown in Online Resource 2 from Fig S2 to Fig S5, and the land cover maps for the images of the validation group are shown in Fig S6 and Fig S7.

3.5 Influence of spatial resolution of land cover maps on runoff results

Figure 16 illustrates an example of the spatial distribution of the grid cell weighted average CN values derived from the both data sources, the UHSR imagery developed in this study, and the CLC database. The results are different according to the first visual interpretation and they show several responses between the categories of land cover. Thus, the spatial distribution of the CN values depends on the spatial resolution of the land cover data source. The CN maps for the all the images used in this study are shown in Fig S8 to Fig S13.

Given that the differences have physical sense, the MAD summarize if the disagreement between each pair means overestimation or underestimation of the CN value. As shown in Fig. 17a, the CLC-CN values below, a threshold value of 66 are smaller than the UHRS-CN values, which means underestimation of the runoff of the CLC for the broad-leaved forest, mixed forest, transitional woodland-shrub, pastures, olive groves and complex cultivation patterns. On the other hand, the CLC-CN values over a threshold value of 66 are higher than the UHRS-CN values, which means overestimation of the runoff for the categories of sclerophyllous vegetation, agro-forestry areas, natural grasslands, non-irrigated arable land, land principally occupied by agriculture, with significant areas of natural vegetation, sparsely vegetated areas, mineral extraction sites and continuous urban fabric. The differences in the estimation of the CN values between the UHSR and CLC (Fig. 17b) reached a RMSD of 6.26. Lastly, it is worth noting that the underestimation in runoff corresponds to the most representative land cover in the *dehesa* environment.

4 Discussion

In this work, the vegetation in a *dehesa* environment was studied using PNOA UHSR imagery considering both the overstory and understory strata. Here, we proposed the use of several UHSR images without the need for mosaic processing, using the information of the bands without further calibration. Therefore, the vegetation was analyzed considering the data available, which resulted in 4 optical bands (NIR, red, green, and blue) and the metrics derived from them, such as VI, SI, and TF.

Our results were presented in two different groups: the training and the validation group. The training group results could be compared to previous works, given that they derived from the application of a traditional process. In this sense, a supervised classification was carried out using the data collected from all the images of the training group. We verified that the ground data could be extracted from each independent tile and merged all data to build a global dataset that could be used for the characterization of land cover categories. Then, we tested our novel approach, which consisted of applying the information of the global dataset of the training group to the validation group, for which ground data extraction was not necessarily performed. The OA and kappa index results (Table 8) were excellent for the training group and very good for the validation group, reaching similar accuracy levels than those obtained in previous studies (Table 2).

Regarding the overstory classification, given that this stratum is mainly comprised of holm oaks, any necessary species discrimination was applied in this work. Therefore, the error matrix statistics for this category were excellent for the training group (Fig. 12) and very good for the validation group (Fig. 13). Importantly, our results were consistent with those reported by Boggs (2010), in which tree canopies were mapped using QuickBird imagery pan-sharpened to a spatial resolution of 0.5 m. In this work, the author used the same spectral bands used herein, but also considered NDVI data, thereby joining two approaches into an NDVI pixel- and object-based image analysis (OBIA). The OA values ranged from 85% to 95% for the NDVI pixel-based approach, and from 87% to 97% for the OBIA. Therefore, our training group results were slightly better than those obtained even with the OBIA approach. Considering other works that used VHSR, our results were comparable to those of Dalponte et al. (2014), which employed a spatial resolution of 0.40 m in their tree crown delineation and tree species classification in boreal forests using hyperspectral images. The best species classification producer's accuracy reached 97.5% for pine trees. Here, the sensitivity for holm oaks reached 98% in both training and validation groups. Moreover, it is important to point out that this was achieved using only 12 predictors in the classification versus the 160 spectral bands of their work, even though no species discrimination was applied in our study.

Regarding the understory classification, particularly the shrub species discrimination, our results were slightly better than those obtained in previous works that focused on understory strata, even though our work used UHSR instead of the more traditionally used VHSR (e.g.,Eroğlu et al. (2010), Malahlela et al. (2015), Niphadkar et al.

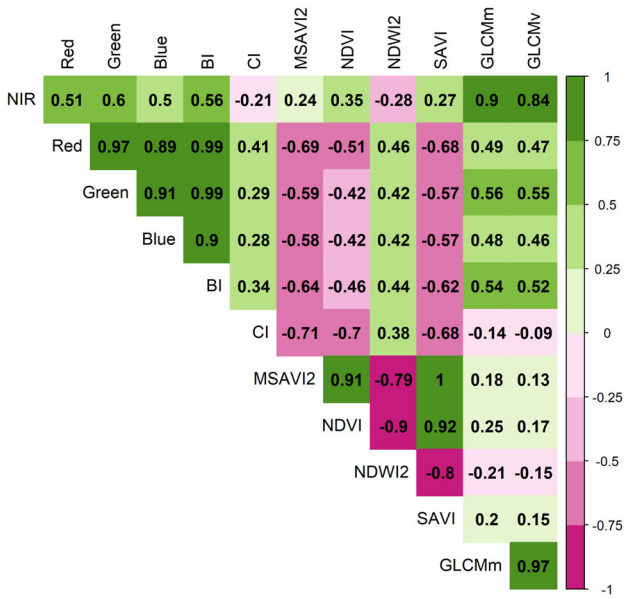

Fig. 18 Pearson correlation coefficient of the predictors

(2017) and van Lier et al. (2009)). Eroğlu et al. (2010) and van Lier et al. (2009) reported an overall accuracy of 82.5% and 79.8% using IKONOS imagery. Similar to our macro-class-level analysis, van Lier et al. (2009) achieved a producer's accuracy of 87.8% for understory strata classification, pointing out that their method was weaker for areas with sparse cover of ericaceous shrubs or dense tree cover. Likewise, our results were better than those of Eroğlu et al. (2010) which reported a producer's accuracy of 65.9% and 93.75% for overstory and understory respectively, although they grouped shrub and herbaceous plants as a unique category. Moreover, Malahlela et al. (2015) used WordView2 imagery to study the probability of occurrence of a specific invasive shrub (*C. odorata*) in forest gaps, and achieved sensitivity, specificity, and precision values of 87%, 86%, and 87%, respectively. Finally, our results were much better than those of Niphadkar et al. (2017), who used Geo-eye and WordView2 imagery to map another invasive shrub (*Lantana camara*) in a tropical forest, with only an overall accuracy of approximately 60%.

Regarding our analysis of water bodies, it is worth noting that the results for water are by far the weakest of all categories for both the training and validation groups, where sensitivity decreased from 0.68 to 0.12. In the training group, the main confusion was between water and shadows, with a 27% confusion rate (Table S2). In the case of the validation group, low accuracies were attributed to the misclassification of 40% of the pixels. Further, confusion with shadows reached 21% and 10% with urban areas (Table S4). The water bodies in our study area were small cattle ponds and were likely misclassified in the validating group due to the considerable variability between the cattle ponds during the image acquisition period (June). This can be attributed to low depths, as well as suspended algae and sludge, all of which affects the surface's spectral response. Thus, even though the waterbody classification accuracy was poor in our specific case study, said surfaces only represented 0.5% of the studied area.

Regarding the importance of the predictors, our results demonstrated that CI, the blue band, GLCMm, and GLCMv were the most important classification parameters. The CI was the most important predictor, given that it was ranked first at the macro-class-level analysis and second at the class level. In turn, this ranking was not far from the blue band, which ranked first in the class level (Fig. 10). In our study, the CI was helpful to distinguish among vegetation categories, even more than the VI, especially for H and S. Moreover, regarding the non-vegetation categories, the CI was by far the most important for I. These results might be related to the fact that CI IQR values in these categories were very narrow. Therefore, a low dispersion was observed in the sample set. Consequently, the inclusion of CI as a predictor improved the discrimination of non-vegetated areas, as reported by Richardson and Wiegand (1977) and Huete and Post (1984). It is well known that the inclusion of VI facilitates the discrimination of vegetation and thus it is commonly used as a predictor (see Table 2). However, in our results, the VI seemed to have less importance. This may be explained by the seasonal phenology pattern typically observed during early summer in Extremadura (i.e., our study region), whereby the herbaceous stratum loses its greenness and evergreen shrubs become less vigorous, and thus the CI and BI become more effective for discrimination. Additionally, as shown in Fig. 18, a negative correlation was observed between the VI and CI, making them less representative.

The importance of the blue band and the texture features (GLCMm and GLCMv) are in concordance with the results of Burnett et al. (2019). In their study, coconut trees and native forests were mapped using WorldView2 images with a pan-sharpened spatial resolution of 0.5 m. The most important features were the coastal and blue band, ranking first and second in the average importance score, respectively. Moreover, different GLCM metrics were also ranked third to eighth. However, SI was not used in said work, and thus cannot be fully compared with ours. Burnett et al. (2019) concluded that the coastal and blue spectral bands facilitated the discrimination between broad vegetation classes in humid tropics. Although the environment in our study was Mediterranean and non-tropical, our results suggest that the blue band also facilitated discrimination, particularly in the shrub stratum (Fig. 10). Furthermore, based on the method described by Burnett et al.

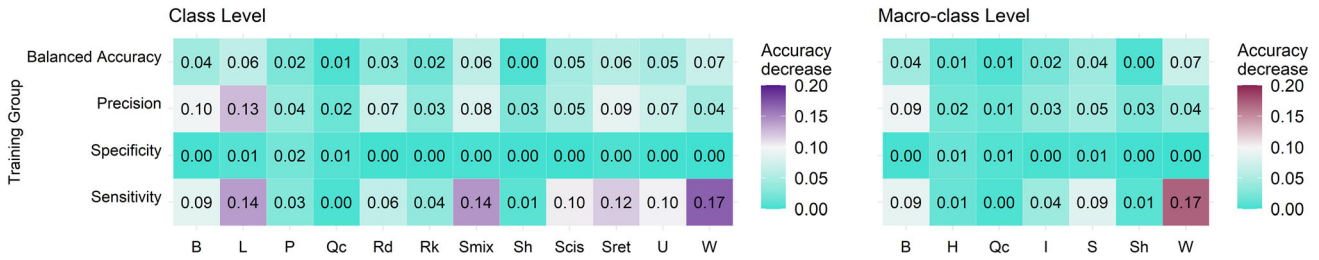

Fig. 19 Evaluation of the classification accuracy measure decreases for each category after eliminating the blue band as a predictor

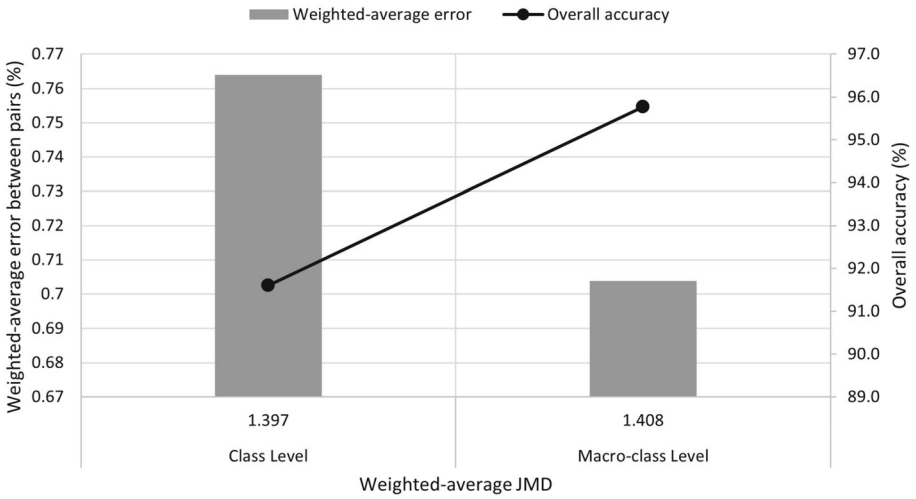

Fig. 20 Weighted-average Jeffries-Matusita distance (JMD) values at both level of analysis, weighted-average error between pairs, and final overall accuracy

(2019), we ran a RF model in the training group without the blue band as a predictor, after which the accuracy decreased at both analysis levels. Specifically, the class-level OA decreased from 91.6% (kappa = 0.89) to 87.8% (kappa = 0.84), and the macro-class-level OA decreased from 95.8% (kappa = 0.94) to 93.5% (kappa = 0.91). Therefore, a general decrease in accuracy metrics was observed in all the categories (Fig. 19).

The most significant decrease was observed in the sensitivity of low strata vegetation (e.g., shrub species) and non-vegetated areas, such as urban areas and water bodies. This was likely because the blue band had a strong positive influence on the classification. Notably, the feature characterization demonstrated that the blue band had different responses within shrub species, and the IQR of the blue band was also very narrow in said categories.

Therefore, it is worth noting that our results confirmed the findings of Burnett et al. (2019) by establishing that the blue band facilitated species discrimination (particularly within shrub species) in a Mediterranean *dehesa* ecosystem. Considering the image acquisition dates, our results are also in agreement with those of Fang et al. (2018), which demonstrated that the blue wavelengths were among the most important variables during spring and summer.

Regarding spectral separability, the JMD was applied in this work. As previously mentioned, the JMD measures the separability between categories and depends on the information that each predictor can provide to the analysis. In our work, the JMD among categories ranged from 1.1 to 1.41 at the class level and from 1.38 to 1.41 at the macro-class level. Reaching a value of 1.41 for most pairs meant that the training data spanned the entire spectral variability between the categories. A low JMD value of 1.1 was observed for the P-L pair, which represented the species in the herbaceous macro-class. In this instance, the feature characterization established no significant differences between herbaceous categories at the class level. On the one hand, the class-level results exhibited a weighted-average confusion error between pairs (considering the 12 categories of the class-level disaggregation analysis) of 0.76%, as well as a related weighted-average JMD value of 1.397. On the other hand, the results at the macro-class level showed a weighted-average error of confusion between pairs (considering the 7 categories) of 0.70% as

well as its related weighted-average JMD value of 1.408 (Fig. 20). In this regard, based on a multiclass JMD analysis, our results demonstrated that higher weighted-average JMD values (considering all categories) translated to lower weighted-average errors between categories. The weighted-average error between pairs was in concordance with the relationship between JMD and the classification error that was mentioned in Lasaponara and Lanorte (2007b) and Lee and Choi (2000), which suggested a classification error probability of approximately 5% or less for a JMD value above 1.24. Additionally, the best OA achieved was related to the higher weighted-average JMD value for the analysis of 7 categories at the macro-class level, which represents an overall misclassification rate of 4.22%. In contrast, the analysis of 12 categories at the class level rendered an overall misclassification rate of 8.4%.

Regarding the tailored maps, we were able to design maps with very high accuracy for the main representative land cover types of the *dehesa* environment. The excellent results obtained for the overstory stratum, which was mainly comprised of holm oaks (*Quercus rotundifolia*) and had a 0.25-m UHSR resolution, allowed us to delineate the tree crown shape with high precision. Thus, the results could be very useful to calculate derived dendometric parameters of individual trees, such as crown area and crown diameter, as well as other dasometric variables related to the tree canopy cover factor and stand density. It is worth noting than shrub species were also classified with high accuracy, allowing us to study shrub cover spatial patterns, which play a crucial role in the hydrologic response of a given territory, as well as pasture productivity and tree growth (Pulido et al. 2010; Rivest et al. 2011), the occurrence of aromatic and medicinal plants and honey (Canteiro et al. 2011) and finally, but not the least important, the management of the *dehesa* ecosystem (Caballero Díaz et al. 2015; Godinho et al. 2016b).

Regarding the influence of the ad hoc land cover maps on the hydrologic process of the territory, the potential response of the UHSR land cover was compared with the potential response derived from a global database such as CLC. Our results, rendered a more precise estimation of the spatial distribution of the CN values, highlighting the influence of the spatial resolution, given that the global data base of CLC underestimate the potential runoff in the most representative land cover in the *dehesa* environment, such as those of broad-leaved forest, mixed forest, transitional woodland-shrub and pastures. This result, was consistent with those reported by Walega and Salata (2019) where the evaluation of the direct runoff using the NRCS-CN method was underestimated compared to the observed events. In this work, the authors pointed out that the differences strongly depend on catchment size due to the risk of over-generalization of the CLC land cover categories. In this regard, further investigation is needed, specially in Mediterranean forested watershed where a regional calibration of the CN is not yet available. Nevertheless, other works in forested areas in United States suggested uncertainties in the application of the CN lookup tables in forested watershed (Tedela et al. 2012; Walega et al. 2020).

For the classification of accurate UHSR land cover maps, the definition of reference data from fieldwork is a time-intensive, expensive, and subjective task (Ghimire et al. 2012). Image photointerpretation techniques could be used to minimize or avoid field campaigns; however, manual processing is also laborious, time-consuming, and impractical for extensive areas (Müllerová et al. 2013). In our work, we have proven the effectiveness of applying a classifier to neighboring images with similar environments that might not participate in the extraction of the training dataset, thereby reducing manual labor. Our approach uses UHSR image spectral information without further calibration, and thus reduces the need for labor-intensive field campaigns, which is especially useful in inaccessible regions. The main limitation of our proposed procedure is that images must have the same flight conditions to ensure the similarity of the spectral information.

Finally, once the UHSR images are classified for both the training and validation groups, the land cover information can be used for the definition of new training datasets for the supervised classification of HSR images, such as Sentinel or Landsat. In this regard, this approach was proposed by Paris et al. (2017) to avoid fieldwork by using the available information from another covering image of the same time series. Their methodology consisted of the definition of a "pseudo" training set from a thematic map analyzing the samples that had the highest probability of belonging to areas where no changes occurred on the ground. Finally, after a validation, these pseudo training samples could be used as training samples for supervised classification.

5 Conclusions

In this study, the vegetation of a *dehesa* environment was studied using PNOA UHSR imagery and a supervised classification algorithm based on the random forest approach. Both the overstory and understory strata were considered to obtain tailored maps of the land cover with high accuracy. During the classification process, the principal predictors were identified, demonstrating how the blue band, soil indices, and texture features were the most important classification parameters. The overstory stratum accuracy results were excellent and shrub species were also classified with high accuracy. This allows us to study shrub cover spatial patterns, which play a crucial role in pasture

productivity and tree growth, the land management of the *dehesa* ecosystem, and the hydrologic response of the territory. Given that the land cover categories were also defined according to the runoff generation capability, the maps could be used as an input for future watershed hydrologic and water balance models. In addition, these maps characterize the environment in a precisely spatial distributed CN values, representing the potential runoff capability of the territory. In this sense, we found that having accurate tailored land cover maps is crucial, given that using a global land cover database, such as CLC, led to underestimating the potential runoff in the most representative land cover in the *dehesa* environment, such as those of broad-leaved forest, mixed forest, transitional woodland-shrub and pastures.

Moreover, we developed a method to reduce field campaigns by evaluating the performance of the classifier to map neighboring images that were not initially used to train the model, achieving good results. Given that our approach uses the spectral information of UHSR images without further calibration, it could be used to minimize the manual labor associated with photointerpretation and field campaigns. Future research will focus on the automatic generation of new samples extracted from classified UHSR images, which could be used as training datasets for the future supervised classification of other HSR images, such as Sentinel imagery. Furthermore, future investigation is also needed to assess the regional calibration of the CN values of HSR land cover images in Mediterranean forested watershed.

Authors' contribution Laura Fragoso-Campón: Conceptualization, Methodology, Software, Formal analysis, Investigation, Writing—Original Draft, Writing—Review & Editing. Elia Quirós: Conceptualization, Methodology, Resources, Writing—Original Draft, Writing—Review & Editing, Supervision. José Antonio Gutiérrez Gallego: Resources, Writing—Review & Editing.

Funding This research was funded by the Junta de Extremadura and the European Social Fund: A way of doing Europe, through the "Financing of Predoctoral Contracts for the Training of Doctors in Public Research and Development Centers belonging to the Extremadura System of Science, Technology, and Innovation [file PD16018]." This work was also supported by the Government of Extremadura (Spain) and co-funded by the European Regional Development Foundation under Grants GR18052 (DESOSTE) and GR18028 (KRAKEN). We thank the Junta de Extremadura (CICTEX) for providing the necessary high-resolution PNOA ortophotographs (PNOA 2007-CC-BY 4.0 scne.es).

Compliance with ethical standards

Conflict of interest The authors declare that they have no known competing financial interests or personal relationships that could have influenced the work reported in this paper.

References

Adam E, Mutanga O, Odindi J, Abdel-Rahman EM (2014) Land-use/cover classification in a heterogeneous coastal landscape using RapidEye imagery: evaluating the performance of random forest and support vector machines classifiers. Int J Remote Sens 35:3440–3458. https://doi.org/10.1080/01431161.2014.903435

Ahmed OS, Franklin SE, Wulder MA, White JC (2015) Characterizing stand-level forest canopy cover and height using Landsat time series, samples of airborne LiDAR, and the random forest algorithm ISPRS. J Photogr Rem Sens 101:89–101. https://doi.org/10.1016/j.isprsjprs.2014.11.007

Akike S, Samanta S (2016) Land use/land cover and forest canopy density monitoring of Wafi-Golpu Project Area Papua New Guinea. J Geosci Environ Prot 4:1. https://doi.org/10.4236/gep.2016.48001

Athira P, Sudheer KP, Cibin R, Chaubey I (2016) Predictions in ungauged basins: an approach for regionalization of hydrological models considering the probability distribution of model parameters. Stochastic Environ Res Risk Assessm 30:1131–1149. https://doi.org/10.1007/s00477-015-1190-6

Becker R, Koppa A, Schulz S, Usman M, Tad Beek, Schüth C (2019) Spatially distributed model calibration of a highly managed hydrological system using remote sensing-derived ET data. J Hydrol 577:123944. https://doi.org/10.1016/j.jhydrol.2019.123944

Boggs GS (2010) Assessment of SPOT 5 and QuickBird remotely sensed imagery for mapping tree cover in savannas. Int J Appl Earth Obs Geoinf 12:217–224. https://doi.org/10.1016/j.jag.2009.11.001

Bolton DK, White JC, Wulder MA, Coops NC, Hermosilla T, Yuan X (2018) Updating stand-level forest inventories using airborne laser scanning and Landsat time series data. Int J Appl Earth Obs Geoinf 66:174–183. https://doi.org/10.1016/j.jag.2017.11.016

Borlaf-Mena I, Tanase MA, Gómez-Sal A (2019) Methods for tree cover extraction from high resolution orthophotos and airborne LiDAR scanning in Spanish dehesas. Revista de Teledetección 1:17–32. https://doi.org/10.4995/raet.2019.11320

Breiman L (2001) Random For Mach Learn 45:5–32. https://doi.org/10.1023/A:1010933404324

Burnett MW, White TD, McCauley DJ, De Leo GA, Micheli F (2019) Quantifying coconut palm extent on Pacific islands using spectral and textural analysis of very high resolution imagery. Int J Remote Sens 40:7329–7355. https://doi.org/10.1080/01431161.2019.1594440

Caballero Díaz J, Pérez F, Manuel A, Quirós Rosado E (2015) A state-and-transition model of Iberian dehesas based on spatial patterns Forest Systems 24:1. https://doi.org/10.5424/fs/2015242-06408

Campos I, Villodre J, Carrara A, Calera A (2013) Remote sensing-based soil water balance to estimate Mediterranean holm oak savanna (dehesa) evapotranspiration under water stress conditions. J Hydrol 494:1–9. https://doi.org/10.1016/j.jhydrol.2013.04.033

Campos I, Gonzalez-Piqueras J, Carrara A, Villodre J, Calera A (2016) Estimation of total available water in the soil layer by integrating actual evapotranspiration data in a remote sensing-driven soil water balance. J Hydrol 534:427–439. https://doi.org/10.1016/j.jhydrol.2016.01.023

Canteiro C, Pinto-Cruz C, Simões MP, Gazarini L (2011) Conservation of Mediterranean oak woodlands: understorey dynamics under different shrub management. Agrofor Syst 82:161–171. https://doi.org/10.1007/s10457-011-9375-6

Cantero Fauquier F, Tomé Morán J, Bravo Fernández J, Fernández-Landa A (2017) Herramientas de localización de árboles

individuales con el módulo de procesado de QGIS a partir de información LiDAR y ortofotografía aérea. Paper presented at the 7° Congreso Forestal Español "Gestión del monte: servicios ambientales y bioeconomía", Plasencia, Cáceres (Spain), 26–30 junio

Carreiras JM, Pereira JM, Pereira JS (2006) Estimation of tree canopy cover in evergreen oak woodlands using remote sensing. For Ecol Manag 223:45–53. https://doi.org/10.1016/j.foreco.2005.10.056

Castillejo-González IL, Medina Guerrero J, García-Ferrer Porras A, Mesas-Carrascosa FJ, Sánchez de la Orden M (2010) Utilización de imágenes de satélite de alta resolución espacial en la determinación de la fracción de cabida cubierta en sistemas adehesados. Paper presented at the XIV Congreso Nacional de Tecnologías de la Información Geográfica La información geográfica al servicio de los ciudadanos: de lo global a lo local, Sevilla (Spain)

Castillo JAA, Apan AA, Maraseni TN, Salmo SG III (2017) Estimation and mapping of above-ground biomass of mangrove forests and their replacement land uses in the Philippines using Sentinel imagery. ISPRS J Photogr Rem Sens 134:70–85. https://doi.org/10.1016/j.isprsjprs.2017.10.016

Ceballos A, Schnabel S (1998) Hydrological behaviour of a small catchment in the dehesa landuse system (Extremadura, SW Spain). J Hydrol 210:146–160. https://doi.org/10.1016/s0022-1694(98)00180-2

Cerda A, Schnabel S, Ceballos A, Gomez-Amelia D (1998) Soil hydrological response under simulated rainfall in the Dehesa land system (Extremadura, SW Spain) under drought conditions Earth Surface Processes and Landforms. J Br Geomorphol Group 23:195–209. https://doi.org/10.1002/(sici)1096-9837(199803)23:3%3c195:aid-esp830%3e3.0.co;2-i

Chen H, Liang Q, Liang Z, Liu Y, Xie S (2019a) Remote-sensing disturbance detection index to identify spatio-temporal varying flood impact on crop production. Agric For Meteorol 269:180–191. https://doi.org/10.1016/j.agrformet.2019.02.002

Chen T et al (2019b) Merging ground and satellite-based precipitation data sets for improved hydrological simulations in the Xijiang River basin of China. Stoch Env Res Risk Assess 33:1893–1905. https://doi.org/10.1007/s00477-019-01731-w

Chymyrov A, Betz F, Baibagyshov E, Kurban A, Cyffka B, Halik U (2018) Floodplain forest mapping with sentinel-2 imagery: case study of Naryn River, Kyrgyzstan. In: Vegetation of central asia and environs. Springer, pp 335–347

Congalton RG, Green K (2008) Assessing the accuracy of remotely sensed data: principles and practices. CRC Press, Boca Raton

Conrad O (2010) SAGA-GIS Module Library Documentation (v2.2.0) Module Majority Filter. http://www.saga-gis.org/saga_tool_doc/2.2.0/grid_filter_6.html. Accessed October 2019

Dalponte M, Ørka HO (2016) varSel: Sequential Forward Floating Selection using Jeffries-Matusita Distance, R package version 0.1 edn

Dalponte M, Bruzzone L, Vescovo L, Gianelle D (2009) The role of spectral resolution and classifier complexity in the analysis of hyperspectral images of forest areas. Remote Sens Environ 113:2345–2355. https://doi.org/10.1016/j.rse.2009.06.013

Dalponte M, Bruzzone L, Gianelle D (2012) Tree species classification in the Southern Alps based on the fusion of very high geometrical resolution multispectral/hyperspectral images and LiDAR data. Remote Sens Environ 123:258–270. https://doi.org/10.1016/j.rse.2012.03.013

Dalponte M, Ørka HO, Ene LT, Gobakken T, Næsset E (2014) Tree crown delineation and tree species classification in boreal forests using hyperspectral and ALS data. Rem Sens Environ 140:306–317. https://doi.org/10.1016/j.rse.2013.09.006

Devesa Alcaraz JA (1995) Vegetación y flora de Extremadura. Universitas Editorial

Dias LCP, Macedo MN, Costa MH, Coe MT, Neill C (2015) Effects of land cover change on evapotranspiration and streamflow of small catchments in the Upper Xingu River Basin Central Brazil. J Hydrol: Region Stud 4:108–122. https://doi.org/10.1016/j.ejrh.2015.05.010

Diaz M, Campos P, Pulido FJ (1997) The Spanish dehesas: a diversity in land-use and wildlife. In: Pain D, Pienkowski M (eds) Farming and birds in Europe. Academic Press, London, pp 178–209

Dionizio EA, Costa MH (2019) Influence of land use and land cover on hydraulic and physical soil properties at the cerrado agricultural frontier. Agriculture 9:24. https://doi.org/10.3390/agriculture9010024

Dou X, Song J, Wang L, Tang B, Xu S, Kong F, Jiang X (2018) Flood risk assessment and mapping based on a modified multi-parameter flood hazard index model in the Guanzhong Urban Area. China Stoch Environ Res Risk Assessm 32:1131–1146. https://doi.org/10.1007/s00477-017-1429-5

Durán-Barroso P, González J, Valdés JB (2016) Improvement of the integration of Soil Moisture Accounting into the NRCS-CN model. J Hydrol 542:809–819. https://doi.org/10.1016/j.jhydrol.2016.09.053

Eriksson HM, Eklundh L, Kuusk A, Nilson T (2006) Impact of understory vegetation on forest canopy reflectance and remotely sensed LAI estimates. Remote Sens Environ 103:408–418. https://doi.org/10.1016/j.rse.2006.04.005

Eroğlu H, Çakır G, Sivrikaya F, Akay AE (2010) Using high resolution images and elevation data in classifying erosion risks of bare soil areas in the Hatila Valley Natural Protected Area Turkey. Stoch Environmental Res Risk Assessment 24:699–704. https://doi.org/10.1007/s00477-009-0356-5

Escadafal R (1993) Remote sensing of soil color: principles and applications. Rem Sens Rev 7:261–279. https://doi.org/10.1080/02757259309532181

Escadafal R, Huete A (1991) Etude des propriétés spectrales des sols arides appliquée à l'amélioration des indices de végétation obtenus par télédétection Comptes rendus de l'Académie des sciences Série 2. Mécanique, Physique, Chimie, Sciences de l'univers, Sciences de la Terre 312:1385–1391

Fang F, McNeil BE, Warner TA, Maxwell AE (2018) Combining high spatial resolution multi-temporal satellite data with leaf-on LiDAR to enhance tree species discrimination at the crown level. Int J Remote Sens 39:9054–9072. https://doi.org/10.1080/01431161.2018.1504343

Fassnacht FE et al (2016) Review of studies on tree species classification from remotely sensed data. Remote Sens Environ 186:64–87. https://doi.org/10.1016/j.rse.2016.08.013

Fassnacht FE, Mangold D, Schaefer J, Immitzer M, Kattenborn T, Koch B, Latifi H (2017) Estimating stand density, biomass and tree species from very high resolution stereo-imagery—towards an all-in-one sensor for forestry applications? Forestry 90:613–631. https://doi.org/10.1093/forestry/cpx014

Ferreira MP, Zortea M, Zanotta DC, Shimabukuro YE (2016) Filho CRdS Mapping tree species in tropical seasonal semi-deciduous forests with hyperspectral and multispectral data. Rem Sens Environ 179:66–78. https://doi.org/10.1016/j.rse.2016.03.021

Ferrer i Juliá M (2003) Análisis de nuevas fuentes de datos para la estimación del parámetro número de curva: perfiles de suelos y teledetección. Monografía C48. CEDEX

Fragoso L, Quirós E, Durán-Barroso P (2017) Resource communication: Variability in estimated runoff in a forested area based on different cartographic data sources. For Syst 26:02

Fragoso-Campón L, Quirós E, Mora J, Gutiérrez Gallego JA, Durán-Barroso P (2019) Overstory-understory land cover mapping at

the watershed scale: accuracy enhancement by multitemporal remote sensing analysis and LiDAR. Environ Sci Pollut Res 1:1–14. https://doi.org/10.1007/s11356-019-04520-8

Franklin J (2010) Mapping species distributions: spatial inference and prediction. Cambridge University Press, New York

Gao B-C (1996) NDWI—A normalized difference water index for remote sensing of vegetation liquid water from space. Remote Sens Environ 58:257–266

Garcia M, Saatchi S, Ferraz A, Silva CA, Ustin S, Koltunov A, Balzter H (2017) Impact of data model and point density on aboveground forest biomass estimation from airborne LiDAR. Carbon Bal Manag 12:4. https://doi.org/10.1186/s13021-017-0073-1

García M, Riaño D, Chuvieco E, Salas J, Danson FM (2011) Multispectral and LiDAR data fusion for fuel type mapping using Support Vector Machine and decision rules. Remote Sens Environ 115:1369–1379. https://doi.org/10.1016/j.rse.2011.01.017

GDAL-documentation (2019) gdal_sieve. https://gdal.org/programs/gdal_sieve.html. Accessed October 2019

Ghimire B, Rogan J, Galiano VR, Panday P, Neeti N (2012) An evaluation of bagging, boosting, and random forests for land-cover classification in Cape Cod, Massachusetts, USA. GISci Rem Sens 49:623–643. https://doi.org/10.2747/1548-1603.49.5.623

Ghosh A, Fassnacht FE, Joshi PK, Koch B (2014) A framework for mapping tree species combining hyperspectral and LiDAR data: role of selected classifiers and sensor across three spatial scales. Int J Appl Earth Obs Geoinf 26:49–63. https://doi.org/10.1016/j.jag.2013.05.017

Godinho S, Gil A, Guiomar N, Costa MJ, Neves N (2016a) Assessing the role of Mediterranean evergreen oaks canopy cover in land surface albedo and temperature using a remote sensing-based approach. Appl Geogr 74:84–94. https://doi.org/10.1016/j.apgeog.2016.07.004

Godinho S et al (2016b) Assessment of environment, land management, and spatial variables on recent changes in montado land cover in southern Portugal. Agrofor Syst 90:177–192. https://doi.org/10.1007/s10457-014-9757-7

Godinho S, Guiomar N, Gil A (2017) Estimating tree canopy cover percentage in a mediterranean silvopastoral systems using Sentinel-2A imagery and the stochastic gradient boosting algorithm International. J Rem Sens 1:1–23. https://doi.org/10.1080/01431161.2017.1399480

Hall-Beyer M (2017) Practical guidelines for choosing GLCM textures to use in landscape classification tasks over a range of moderate spatial scales. Int J Remote Sens 38:1312–1338. https://doi.org/10.1080/01431161.2016.1278314

Haralick RM, Shanmugam K (1973) Textural features for image classification. IEEE Trans Syst Man Cybern 1:610–621. https://doi.org/10.1109/tsmc.1973.4309314

Hastie T, Tibshirani R, Friedman J (2009) The elements of statistical learning: data mining, inference, and prediction. Springer, Berlin, pp 587–601. https://doi.org/10.1007/b94608

Hawryło P, Wężyk P (2018) Predicting growing stock volume of scots pine stands using Sentinel-2 satellite imagery and airborne image-derived point clouds. Forests 9:274. https://doi.org/10.3390/f9050274

Hernández-López D, Felipe-García B, González-Aguilera D, Arias-Pérez B (2013) Web-based spatial data infrastructure: a solution for the sustainable management of thematic information supported by aerial orthophotography. Dyna 80:123–131

Hijmans RJ (2019) raster: Geographic Data Analysis and Modeling., R package version 2.9-5. edn

Huete A (1988) A soil-adjusted vegetation index (SAVI). Remote Sens Environ 25:259–309. https://doi.org/10.1016/0034-4257(88)90106-x

Huete AR, Post DF (1984) Jackson RD (1984) Soil spectral effects on 4-space vegetation discrimination. Remote Sens Environ 15(2):155–165. https://doi.org/10.1016/0034-4257(84)90043-9

IGN Centro de Descargas. Centro Nacional de Información Geográfica. http://centrodedescargas.cnig.es/CentroDescargas/index.jsp. Accessed Julio 2019

Immitzer M, Vuolo F, Atzberger C (2016) First experience with Sentinel-2 data for crop and tree species classifications in central Europe. Remote Sens 8:166. https://doi.org/10.3390/rs8030166

Joffre R, Rambal S (1993) How tree cover influences the water balance of Mediterranean rangelands. Ecology 74:570–582. https://doi.org/10.2307/1939317

Kim S-R, Lee W-K, Kwak D-A, Biging G, Gong P, Lee J-H, Cho H-K (2011) Forest cover classification by optimal segmentation of high resolution satellite imagery. Sensors 11:1943–1958. https://doi.org/10.3390/s110201943

Kuhn M et al. (2018) caret: Classification and Regression Training., R package version 6.0-81. edn

Labrador García M, Évora Brondo JA, Arbelo Pérez M (2012) Satélites de Teledetección para la Gestión del Territorio

Landry S, St-Laurent M-H, Nelson PR, Pelletier G, Villard M-A (2018) Canopy cover estimation from landsat images: understory impact ontop-of-canopy reflectance in a northern hardwood forest. Can J Remote Sens 44:435–446. https://doi.org/10.1080/07038992.2018.1533399

Lasaponara R, Lanorte A (2007) On the capability of satellite VHR QuickBird data for fuel type characterization in fragmented landscape. Ecol Model 204:79–84. https://doi.org/10.1016/j.ecolmodel.2006.12.022

Lasaponara R, Lanorte A On the spectral separability of Prometheus fuel types in the Mediterranean ecosystems of the Italian Peninsula. In: Gitas I, Carmona-Moreno C (eds) Proceedings of the 6th International Workshop of The EARSeL Special Interest Group On Forest Fires—Advances in Remote Sensing and GIS Applications in Forest Fire Management: Towards An Operational Use of Remote Sensing in Forest Fire Management, Thessaloniki (Greece) 27–29 September 2007 2007b. European Commission. Joint Research Centre. Institute for Environment and Sustainability, pp 115–118

Lavado Contador JF, Jariego García A, Schnabel S, Gómez Gutiérrez Á (2012) Análisis de la evolución histórica del arbolado de la dehesa mediante fotointerpretación y análisis OBIA. Paper presented at the Tecnologías de la información geográfica en el contexto del cambio global: XV Congreso Nacional de Tecnologías de Información Geográfica, Madrid (Spain), 19 al 21 de septiembre de 2012

Lee C, Choi E (2000) Bayes error evaluation of the Gaussian ML classifier. IEEE Trans Geosci Remote Sens 38:1471–1475. https://doi.org/10.1109/36.843045

Li A et al (2017) Lidar aboveground vegetation biomass estimates in shrublands: prediction, uncertainties and application to coarser scales. Remote Sens 9:903. https://doi.org/10.3390/rs9090903

Liaw A, Wiener M (2002) Classification and Regression by random. Forest

Lima de Almeida C, Anchiêta de Carvalho TR, de Araújo JC (2019) Leaf area index of Caatinga biome and its relationship with hydrological and spectral variables. Agric For Meteorol 279:107705. https://doi.org/10.1016/j.agrformet.2019.107705

Magiera A, Feilhauer H, Tephnadze N, Waldhardt R, Otte A (2016) Separating reflectance signatures of shrub species—a case study in the Central Greater Caucasus. Appl Veg Sci 19:304–315. https://doi.org/10.1111/avsc.12205

Malahlela OE, Cho MA, Mutanga O (2015) Mapping the occurrence of Chromolaena odorata (L) in subtropical forest gaps using environmental and remote sensing data. Biol Invas 17:2027–2042. https://doi.org/10.1007/s10530-015-0858-7

Mas J-F, Gao Y, Navarrete Pacheco JA (2010) Sensitivity of landscape pattern metrics to classification approaches. For Ecol Manag 259:1215–1224. https://doi.org/10.1016/j.foreco.2009.12.016

Mathieu R, Pouget M, Cervelle B, Escadafal R (1998) Remote Sens Environ 66:17–28. https://doi.org/10.1016/S0034-4257(98)00030-3

Melesse AM, Shih SF (2002) Spatially distributed storm runoff depth estimation using Landsat images and GIS. Comput Electron Agric 37:173–183. https://doi.org/10.1016/S0168-1699(02)00111-4

Ministerio de Fomento (2016) Instrucción de Carreteras norma 5.2 - IC drenaje superficial

Ministerio de Fomento (2019) Plan Nacional de Observación del Territorio. Plan Nacional de Ortofotografía Aerea (PNOA). http://pnoa.ign.es/presentacion. Accessed 22 abril 2019

Müllerová J, Pergl J, Pyšek P (2013) Remote sensing as a tool for monitoring plant invasions: testing the effects of data resolution and image classification approach on the detection of a model plant species Heracleum mantegazzianum (giant hogweed) International. J Appl Earth Observ Geoinf 25:55–65. https://doi.org/10.1016/j.jag.2013.03.004

Mura M et al (2018) Exploiting the capabilities of the Sentinel-2 multi spectral instrument for predicting growing stock volume in forest ecosystems. Int J Appl Earth Obs Geoinf 66:126–134. https://doi.org/10.1016/j.jag.2017.11.013

Netzer MS, Sidman G, Pearson TR, Walker SM, Srinivasan R (2019) Combining global remote sensing products with hydrological modeling to measure the impact of tropical forest loss on water-based ecosystem services. Forests 10:413. https://doi.org/10.3390/f10050413

Niphadkar M, Nagendra H, Tarantino C, Adamo M, Blonda P (2017) Comparing pixel and object-based approaches to map an understorey invasive shrub in tropical mixed forests Frontiers in plant science 8:892. https://doi.org/10.3389/fpls.2017.00892

Niu J, Sivakumar B (2014) Study of runoff response to land use change in the East River basin in South China. Stochastic Environ Res Risk Assessment 28:857–865. https://doi.org/10.1007/s00477-013-0690-5

Nizami SM, Yiping Z, Zheng Z, Zhiyun L, Guoping Y, Liqing S (2017) Evaluation of forest structure, biomass and carbon sequestration in subtropical pristine forests of SW China. Environ Sci Pollut Res 24:8137–8146. https://doi.org/10.1007/s11356-017-8506-7

Nomura K, Mitchard E (2018) More than meets the eye: using sentinel-2 to map small plantations in complex forest landscapes. Remote Sens 10:1693. https://doi.org/10.3390/rs10111693

NRCS (2004) Chapter 9: hydrologic soil-cover complexes. In: NRCS National engineering handbook, Part 630: Hydrology. Engineering Division, US. Department of Agriculture, Washington, DC

NRCS (2009) National Engineering Handbook, section 4, Hydrology, version (1956, 1964, 1971, 1985, 1993, 2004, 2009). National Engineering Handbook. Engineering Division, US. Department of Agriculture, Washington, DC

Olea L, San Miguel-Ayanz A The Spanish dehesa. A traditional Mediterranean silvopastoral system linking production and nature conservation. In: Sustainable Grassland Productivity, Badajoz (Spain), 2006. Sociedad Española para el Estudio de los Pastos (S.E.E.P.), pp 3–13

Olea L, López-Bellido R, Poblaciones M (2005) European types of silvopastoral systems in the Mediterranean area: dehesa Silvopastoralism and sustainable land management CABI. Oxfordshire 1:30–35

Paris C, Bruzzone L, Fernández-Prieto D A novel automatic approach to the update of land-cover maps by unsupervised classification of remote sensing images. In: Geoscience and Remote Sensing Symposium (IGARSS), 2017 IEEE International, 2017. IEEE, pp 2207–2210. https://doi.org/10.1109/igarss.2017.8127426

Petroselli A, Grimaldi S (2018) Design hydrograph estimation in small and fully ungauged basins: a preliminary assessment of the EBA4SUB framework. J Flood Risk Manag 11:S197–S210. https://doi.org/10.1111/jfr3.12193

Psomiadis E, Soulis KX, Efthimiou N (2020) Using SCS-CN and earth observation for the comparative assessment of the hydrological effect of gradual and abrupt spatiotemporal land cover changes. Water 12:1386. https://doi.org/10.3390/w12051386

Pulido F, García E, Obrador JJ, Moreno G (2010) Multiple pathways for tree regeneration in anthropogenic savannas: incorporating biotic and abiotic drivers into management schemes. J Appl Ecol 47:1272–1281. https://doi.org/10.1111/j.1365-2664.2010.01865.x

Pulido-Fernández M, Schnabel S, Lavado-Contador JF, Mellado IM, Pérez RO (2013) Soil organic matter of Iberian open woodland rangelands as influenced by vegetation cover and land management. CATENA 109:13–24. https://doi.org/10.1016/j.catena.2013.05.002

Qi J, Chehbouni A, Huete A, Kerr Y, Sorooshian S (1994) A modified soil adjusted vegetation index Remote sensing of environment 48:119–126. https://doi.org/10.1016/0034-4257(94)90134-1

Qi Z-F, Ye X-Y, Zhang H, Yu Z-L (2014) Land fragmentation and variation of ecosystem services in the context of rapid urbanization: the case of Taizhou city. China Stochastic environmental research and risk assessment 28:843–855. https://doi.org/10.1007/s00477-013-0721-2

R-Core-Team (2018) R: A language and environment for statistical computing. R Foundation for Statistical Computing, Vienna (Austria)

Riaño D et al (2007) Estimation of shrub height for fuel-type mapping combining airborne LiDAR and simultaneous color infrared ortho imaging. Int J Wildland Fire 16:341–348. https://doi.org/10.1071/WF06003

Richardson AJ, Wiegand C (1977) Distinguishing vegetation from soil background information. Photogram Eng Remote Sens 43:1541–1552

Rivas-Martinez S, Rivas-Saenz S (1996-2019) Worldwide Bioclimatic Classification System. http://www.globalbioclimatics.org/form/tb_map/index.htm. Accessed July 2019

Rivest D, Rolo V, López-Díaz L, Moreno G (2011) Shrub encroachment in Mediterranean silvopastoral systems: retama sphaerocarpa and Cistus ladanifer induce contrasting effects on pasture and Quercus ilex production. Agric Ecosyst Environ 141:447–454. https://doi.org/10.1016/j.agee.2011.04.018

Rodriguez-Veiga P, Wheeler J, Louis V, Tansey K, Balzter H (2017) Quantifying forest biomass carbon stocks from space. Curr For Rep 3:1–18. https://doi.org/10.1007/s40725-017-0052-5

Rouse Jr J, Haas R, Schell J, Deering D (1974) Monitoring vegetation systems in the Great Plains with ERTS. Paper presented at the Third Earth Resources Technology Satellite-1 Symposium, Washington, DC

Santos-Silva C, Gonçalves A, Louro R (2011) Canopy cover influence on macrofungal richness and sporocarp production in montado ecosystems. Agrofor Syst 82:149–159. https://doi.org/10.1007/s10457-011-9374-7

Stavrakoudis D, Dragozi E, Gitas I, Karydas C (2014) Decision fusion based on hyperspectral and multispectral satellite imagery for accurate forest species mapping. Remote Sens 6:6897–6928. https://doi.org/10.3390/rs6086897

Su T-C (2016) A filter-based post-processing technique for improving homogeneity of pixel-wise classification data. Eur J Rem Sens 49:531–552. https://doi.org/10.5721/EuJRS20164928

Tedela NH et al (2012) Runoff Curve Numbers for 10 small forested watersheds in the mountains of the Eastern United States. J Hydrol Eng 17:1188–1198. https://doi.org/10.1061/(asce)he.1943-5584.0000436

Tuanmu M-N, Viña A, Bearer S, Xu W, Ouyang Z, Zhang H, Liu J (2010) Mapping understory vegetation using phenological characteristics derived from remotely sensed data. Remote Sens Environ 114:1833–1844. https://doi.org/10.1016/j.rse.2010.03.008

Van der Sande C, De Jong S, De Roo A (2003) A segmentation and classification approach of IKONOS-2 imagery for land cover mapping to assist flood risk and flood damage assessment. Int J Appl Earth Obs Geoinf 4:217–229. https://doi.org/10.1016/s0303-2434(03)00003-5

van Lier OR, Fournier RA, Bradley RL, Thiffault N (2009) A multi-resolution satellite imagery approach for large area mapping of ericaceous shrubs in Northern Quebec, Canada International. J Appl Earth Observ Geoinf 11:334–343. https://doi.org/10.1016/j.jag.2009.05.003

Vila-García D, Gil-Docampo M, Iniesto-Alba M (2015) Change detection in land use from unsupervised classifications for updating SIOSE. Implem Galicia Revista de Teledetección 1:63–76. https://doi.org/10.4995/raet.2015.3409

Walega A, Salata T (2019) Influence of land cover data sources on estimation of direct runoff according to SCS-CN and modified SME methods. CATENA 172:232–242. https://doi.org/10.1016/j.catena.2018.08.032

Walega A, Amatya DM, Caldwell P, Marion D, Panda S (2020) Assessment of storm direct runoff and peak flow rates using improved SCS-CN models for selected forested watersheds in the Southeastern United States. J Hydrol Reg Stud 27:100645. https://doi.org/10.1016/j.ejrh.2019.100645

Wang H et al (2019) Landscape-level vegetation classification and fractional woody and herbaceous vegetation cover estimation over the dryland ecosystems by unmanned aerial vehicle platform. Agric For Meteorol 278:107665. https://doi.org/10.1016/j.agrformet.2019.107665

Zhao Y et al (2016) Detailed dynamic land cover mapping of Chile: Accuracy improvement by integrating multi-temporal data. Remote Sens Environ 183:170–185. https://doi.org/10.1016/j.rse.2016.05.016

Zhou P, Huang J, Pontius RG, Hong H (2014) Land classification and change intensity analysis in a coastal watershed of Southeast China. Sensors 14:11640–11658. https://doi.org/10.3390/s140711640